

Phase-field-based lattice Boltzmann model for incompressible binary fluid systems with density and viscosity contrasts

Y. Q. Zu and S. He*

Department of Mechanical Engineering, University of Sheffield, Sheffield S1 3JD, United Kingdom

(Received 4 October 2012; revised manuscript received 8 March 2013; published 3 April 2013)

A lattice Boltzmann model (LBM) is proposed based on the phase-field theory to simulate incompressible binary fluids with density and viscosity contrasts. Unlike many existing diffuse interface models which are limited to density matched binary fluids, the proposed model is capable of dealing with binary fluids with moderate density ratios. A new strategy for projecting the phase field to the viscosity field is proposed on the basis of the continuity of viscosity flux. The new LBM utilizes two lattice Boltzmann equations (LBEs): one for the interface tracking and the other for solving the hydrodynamic properties. The LBE for interface tracking can recover the Chan-Hilliard equation without any additional terms; while the LBE for hydrodynamic properties can recover the exact form of the divergence-free incompressible Navier-Stokes equations avoiding spurious interfacial forces. A series of 2D and 3D benchmark tests have been conducted for validation, which include a rigid-body rotation, stationary and moving droplets, a spinodal decomposition, a buoyancy-driven bubbly flow, a layered Poiseuille flow, and the Rayleigh-Taylor instability. It is shown that the proposed method can track the interface with high accuracy and stability and can significantly and systematically reduce the parasitic current across the interface. Comparisons with momentum-based models indicate that the newly proposed velocity-based model can better satisfy the incompressible condition in the flow fields, and eliminate or reduce the velocity fluctuations in the higher-pressure-gradient region and, therefore, achieve a better numerical stability. In addition, the test of a layered Poiseuille flow demonstrates that the proposed scheme for mixture viscosity performs significantly better than the traditional mixture viscosity methods.

DOI: [10.1103/PhysRevE.87.043301](https://doi.org/10.1103/PhysRevE.87.043301)

PACS number(s): 47.55.-t, 47.11.St

I. INTRODUCTION

Numerical modeling of multiphase fluid flows plays an important role in solving many applied science and engineering problems, including, for example, oil and gas production, chemical processing, and steam-water mixture flow in boilers and condensers. Major challenges include simulations of phase segregation and interfacial dynamics. Interface tracking is widely used in two-phase flow models, which can be divided into two categories: sharp interface methods, such as volume-of-fluid [1], level-set [2], and front-tracking [3] methods, and diffuse interface methods [4–8]. The latter has some advantages over the former in terms of maintaining mass conservation and being able to resolve interface curvature with higher accuracy. The basic idea of the diffuse interface models is to replace the sharp interfaces with thin but nonzero thickness transitional regions where the density, viscosity, and other physical quantities vary smoothly from the values of one fluid to those of the other. Among the diffuse interface methods, the phase-field method has become a widely used technique in conventional computational fluid dynamics (CFD) [5,6] and lattice Boltzmann methods (LBM) [9–11] to numerically investigate complex interfacial dynamics. In the phase-field method, the thermodynamic behavior of fluids is expressed using the free-energy functional of a continuous order parameter, which acts as a phase field to distinguish the different fluids. An interface-capturing equation is formulated for the order parameter which mimics the Cahn-Hilliard equation.

In the past two decades, the LBM has been established as an effective numerical scheme for simulating multiphase fluid flows. It can be categorized as a diffuse interface approach, albeit differing significantly from “conventional” continuum-based CFD. The key idea behind the LBM is to indirectly recover the correct macroscopic motion of fluid of the complicated physical problem through simulations of simplified microscopic models or mesoscopic kinetic equations. In this method, the kinetic equations for particle distribution function are solved and macroscopic quantities are obtained by evaluating the hydrodynamic moments of the distribution function. By incorporating intermolecular interactions at the mesoscopic level, the LBM is able to model the phase segregation and the interfacial dynamics of multiphase flow [12–15], which are difficult to handle by use of conventional CFD methods. The LBM has been demonstrated to be highly versatile and having significant potentials and broad applicability with many computational advantages, including easy parallelization [16] and boundary treatment [17].

Gunstensen *et al.* [18] proposed the first multiphase flow LBM model, known as the chromodynamic model, based on the two-component lattice gas method [19]. In this model, two-particle distributions, say red and blue, are introduced for the two different fluids, respectively. An additional collision operator is introduced to model the surface tension effects at the interface, and a color-redistribution step is utilized after a collision to enforce the phase segregation. Grunau *et al.* [20] improved this model to allow variations of density and viscosity. Later, Shan and Chen [21] proposed a new multiphase LBM model by incorporating pseudopotentials representing attractive or repulsive forces into an additional

*Corresponding author: s.he@sheffield.ac.uk

collision operator to mimic the molecular potential. The model returns a nonideal equation of state. Phase separation takes place spontaneously whenever the interaction strength exceeds a critical value. Subsequently, Swift *et al.* [10,22] proposed a LBM model for multiphase and multicomponent flows using the idea of free energy. The main feature of this model is the direct inclusion of a nonideal pressure tensor and an external chemical potential instead of the introduction of the additional collision operator. A shortcoming of this model is that it suffers from the lack of Galilean invariance. Several improved free-energy models have been developed [23,24] to restore the Galilean invariance. More recently, Inamuro *et al.* [25] have proposed a free-energy LBM for incompressible two-phase flows with large density ratios. He *et al.* [26] developed a different type of model, which is referred to as the index function model, to simulate incompressible multiphase flow. They employed two distribution functions, one of which calculates the velocity and pressure fields and the other evaluates the index function to track the interfaces between different fluids. In the low-frequency limit, the divergence-free condition of velocity can be approximately satisfied by the model. Later, Lee and Lin [27] developed a three-stage stable discretization scheme for the index function model [26] by discretizing the gradient terms in different manners before and after the streaming step so the multiphase flow with a large density ratio can be simulated.

In the above-mentioned multiphase models for incompressible or weakly compressible binary fluids, the interface between the different phases is tracked by a LBE for either an order parameter [10,25] or an index function [26,27]. Unfortunately, Zheng *et al.* [8,28] found that the interface capturing equation in all of these models cannot completely recover the convective Cahn-Hilliard equation [5,29–33]. To overcome this limitation, they proposed a new LBE for interface capturing [8] which can recover the Cahn-Hilliard equation exactly. Combining this LBE for tracing the interface and a free-energy LBE for solving velocity field, they presented a new LBM for multiphase flow [28]. Although the authors initially claimed that the method could deal with two fluids with large density ratios, Fakhari and Rahimian [11] recently found that the method is suitable only for density-matched binary fluids in which the Boussinesq approximation holds. In fact, many existing LBMs for binary fluids [9,10,28,34,35] are limited to density-matched fluids. This is not a good representation of a real two-phase system. Fakhari and Rahimian [11] proposed a multi-relaxation-time LBM combining the LBE of Zheng *et al.* [8] for interface capturing with the LBE of He *et al.* [26] for the velocity and pressure fields. This model is capable of simulating multiphase flows with moderate density ratios and being consistent with the Cahn-Hilliard equation. However, they found that the stability of their model is very sensitive to the value of mobility in the interface capturing. This remains to be a major limitation of this promising method. Very recently, Li *et al.* [33] discussed another common limitation of existing LBM models for binary fluids that needs addressing, namely the recovered momentum equations of most models are inconsistent with the target momentum equation of incompressible multiphase flows. In these models, there exists an artificial interfacial force proportional to the macroscopic velocity, which is theoretically

small. However, Li *et al.* [33] found that, with the increase of velocity, the effects of the artificial interfacial force on the prediction of the interface can increase significantly, resulting in high numerical uncertainties.

In the work reported herein, we propose a new LBM model for incompressible binary fluids to address a number of limitations of existing LBMs for binary fluid systems discussed above. The model utilizes two LBEs: one for the interface capturing and the other for resolving hydrodynamic properties. The LBE for interface capturing is developed following the basic idea of Zheng *et al.* [8], the performance of which is significantly improved by introducing several modifications. In the LBE for hydrodynamic properties, new equilibrium particle distribution functions are proposed which recover fluid velocity-based macrodynamic equations rather than the fluid momentum-based ones as used in most of the existing LBM models [10,11,26,33]. It will be shown that the former is advantageous over the latter in dealing with the incompressible condition. The new model has the following features: (i) the LBE for the interface capturing can exactly recover the Cahn-Hilliard equation and performs better than previous methods tested in terms of accuracy and stability; (ii) the LBE for hydrodynamic properties is able to recover the divergence-free incompressible Navier-Stokes (N-S) equation in a form advantageous than previous models by using a velocity-based formulation; and (iii) the model is capable of truthfully representing two fluids with moderate density and viscosity ratios.

The rest of the paper is organized as follows. In Sec. II, the methodology of the newly proposed LBEs for binary fluid systems based on phase-field theory is introduced; the macrodynamic behavior arising from the LBEs is derived and compared with the target equations in the phase-field theory. Section III is then devoted to verifying the performance of the model using a variety of benchmark problems, followed by conclusions given in Sec. IV.

II. PHASE-FIELD-BASED LBM FOR BINARY FLUIDS

A. Phase-field theory

The new method developed is based on the phase-field method, a brief outline of which is given in this subsection to facilitate the discussion. A more detailed account of the method can be found in Refs. [5,36]. The phase-field method is a particular class of diffuse-interface model. In this method, an order parameter ϕ is used to distinguish the different fluids, and a Landau free-energy function [36] is defined as

$$\Psi = \int_V dV [\psi(\phi) + k |\nabla\phi|^2 / 2], \quad (1)$$

where the square of the gradient term on the right-hand side of the equation provides an excess free energy in the interfacial region which defines the surface energy, V is the control volume, k the coefficient of surface tension, and $\psi(\phi)$ the bulk free-energy density. For an isothermal system, the following double-well form of free-energy density [5,32] can be used:

$$\psi(\phi) = \beta(\phi - \phi_A)^2(\phi - \phi_B)^2, \quad (2)$$

where β is a constant dependent on the interfacial thickness and the surface tension force. ϕ_A and ϕ_B are constants

corresponding to the equilibrium state, i.e., the order parameters to mark the bulk fluids A and B, respectively. Normally, their values are chosen as $\phi_A = -\phi_B$ [5,11,32,33].

The variation of the free-energy function Ψ with respect to the order parameter yields the chemical potential [5,32,37],

$$\begin{aligned}\mu_\phi &= \frac{\delta\Psi}{\delta\phi} = \frac{\partial\psi}{\partial\phi} - k\nabla^2\phi \\ &= 4\beta(\phi - \phi_A)(\phi - \phi_B)(\phi - \bar{\phi}) - k\nabla^2\phi,\end{aligned}\quad (3)$$

where $\bar{\phi} = (\phi_A + \phi_B)/2$. The equilibrium interface profile then can be obtained by minimizing $\Psi(\phi)$ with respect to the function ϕ , i.e., solving $\mu_\phi(\phi) = 0$. In a plane interface at the equilibrium condition, the order-parameter profile across the interface is represented as [37]

$$\phi(\zeta) = \frac{\phi_A + \phi_B}{2} + \frac{\phi_A - \phi_B}{2} \tanh\left(\frac{2\zeta}{W}\right),\quad (4)$$

where ζ is the coordinate normal to the interface and the interface thickness W is given by [5,32,37],

$$W = \frac{4}{|\phi_A - \phi_B|} \sqrt{\frac{k}{2\beta}}.\quad (5)$$

The fluid-fluid surface tension force σ_{AB} is given in Refs. [31,37] as

$$\sigma_{AB} = \frac{|\phi_A - \phi_B|^3}{6} \sqrt{2k\beta}.\quad (6)$$

Cahn and Hilliard [29,30] generalized the problem to time-dependent situations by approximating interfacial diffusion fluxes as being proportional to chemical potential gradients so as to enforce the conservation of the field. Thus, the time-dependent interface profile can be described in term of ϕ field governed by the convective Cahn-Hilliard equation [5,29–33],

$$\frac{\partial\phi}{\partial t} + \nabla \cdot (\phi\mathbf{u}) = M\nabla^2\mu_\phi,\quad (7)$$

where \mathbf{u} and t are the velocity and time, respectively, and M is a diffusion parameter named as mobility.

In the phase-field method, the hydrodynamic equations for incompressible multiphase flows are given by [6,7,33,34]

$$\nabla \cdot \mathbf{u} = 0,\quad (8a)$$

$$\rho \frac{\partial \mathbf{u}}{\partial t} + \rho \nabla \cdot (\mathbf{u}\mathbf{u}) = -\nabla p_h + \nabla \cdot \Pi + \mathbf{F}_s + \mathbf{F}_b.\quad (8b)$$

In Eq. (8b), ρ is the density of fluids; p_h represents the hydrodynamic pressure which enforces the incompressibility condition; $\Pi = \mu(\nabla\mathbf{u} + \mathbf{u}\nabla)$ is the viscous stress tensor, where μ is the dynamic viscosity; \mathbf{F}_s is the force associated with surface tension, and \mathbf{F}_b is the body force. In this study, a potential form of the surface tension $\mathbf{F}_s = -\phi\nabla\mu_\phi$ is used to reduce the parasitic currents across the interface of the fluids [38].

For an incompressible flow, the divergence-free condition, i.e., Eq. (8a) is satisfied so that Eq. (7) can be rewritten as

$$\frac{\partial\phi}{\partial t} + \mathbf{u} \cdot \nabla\phi = M\nabla^2\mu_\phi.\quad (9)$$

B. LBE for incompressible hydrodynamic equations: A velocity-based method

We start from a standard form of LBE for hydrodynamic properties including velocity and pressure, which reads

$$\begin{aligned}f_\alpha(\mathbf{x} + \mathbf{e}_\alpha\delta t, t + \delta t) - f_\alpha(\mathbf{x}, t) \\ = -\frac{f_\alpha(\mathbf{x}, t) - f_\alpha^{\text{eq}}(\mathbf{x}, t)}{\tau_f} + \frac{2\tau_f - 1}{2\tau_f} F_\alpha\delta t.\end{aligned}\quad (10)$$

In the above equation, \mathbf{x} and t are the space coordinate and time, \mathbf{e}_α is particle velocity in the α th direction, $f_\alpha(\mathbf{x}, t)$ is a particle distribution function along the α th direction, $f_\alpha^{\text{eq}}(\mathbf{x}, t)$ is its corresponding equilibrium state, τ_f is dimensionless relaxation time for velocity field, δt is a time step, and F_α is a distribution function for the force term.

In the present study, the two-dimensional nine-velocity (D2Q9) and three-dimensional fifteen-velocity (D3Q15) LBM structures are used to solve flow fields in 2D and 3D, respectively. The particle velocity, \mathbf{e}_α , in D2Q9 and D3Q15 structures can be given by Eqs. (11a) and (11b), respectively,

$$\begin{aligned}[\mathbf{e}_0, \mathbf{e}_1, \mathbf{e}_2, \mathbf{e}_3, \mathbf{e}_4, \mathbf{e}_5, \mathbf{e}_6, \mathbf{e}_7, \mathbf{e}_8] \\ = \begin{bmatrix} 0 & 1 & 1 & 0 & -1 & -1 & -1 & 0 & 1 \\ 0 & 0 & 1 & 1 & 1 & 0 & -1 & -1 & -1 \end{bmatrix} c,\end{aligned}\quad (11a)$$

$$\begin{aligned}[\mathbf{e}_0, \mathbf{e}_1, \mathbf{e}_2, \mathbf{e}_3, \mathbf{e}_4, \mathbf{e}_5, \mathbf{e}_6, \mathbf{e}_7, \mathbf{e}_8, \mathbf{e}_9, \mathbf{e}_{10}, \mathbf{e}_{11}, \mathbf{e}_{12}, \mathbf{e}_{13}, \mathbf{e}_{14}] \\ = \begin{bmatrix} 0 & 1 & 0 & 0 & -1 & 0 & 0 & 1 & -1 & 1 & 1 & -1 & 1 & -1 & -1 \\ 0 & 0 & 1 & 0 & 0 & -1 & 0 & 1 & 1 & -1 & 1 & -1 & -1 & 1 & -1 \\ 0 & 0 & 0 & 1 & 0 & 0 & -1 & 1 & 1 & 1 & -1 & -1 & -1 & 1 & 1 \end{bmatrix} c,\end{aligned}\quad (11b)$$

where c is the streaming speed defined as $c \equiv \delta x/\delta t$, where δx is the streaming length.

To improve the performance of LBMs in recovering the incompressible flow condition, we introduce the following set of relations to be complied by the zeroth, first, and second moments of the equilibrium distribution function, $f_\alpha^{\text{eq}}(\mathbf{x}, t)$:

$$\sum_\alpha f_\alpha^{\text{eq}} = 0; \sum_\alpha f_\alpha^{\text{eq}} \mathbf{e}_\alpha = \mathbf{u}; \sum_\alpha f_\alpha^{\text{eq}} \mathbf{e}_\alpha \mathbf{e}_\alpha = \mathbf{u}\mathbf{u} + p\mathbf{I},\quad (12)$$

where $p = p_h/\rho$. These relations were used by Guo *et al.* [39,40] to reinforce the incompressible conditions truthfully for *single-phase* fluids.

Note that the first moment of the equilibrium distribution functions used here is based on the fluid velocity rather than the fluid momentum; the latter is used in most of the existing LBM models [10,11,26,33], where $\sum_\alpha f_\alpha^{\text{eq}} \mathbf{e}_\alpha = \rho\mathbf{u}$. Therefore, we refer to the new method as velocity-based method and the latter as momentum-based methods.

To satisfy Eq. (12), we introduce the following equilibrium distribution function

$$f_\alpha^{\text{eq}} = \begin{cases} -(1 - \omega_0)\frac{p}{c_s^2} - \omega_0\frac{\mathbf{u} \cdot \mathbf{u}}{2c_s^2}, & \alpha = 0 \\ \omega_\alpha \left[\frac{p}{c_s^2} + \frac{\mathbf{e}_\alpha \cdot \mathbf{u}}{c_s^2} + \frac{(\mathbf{e}_\alpha \cdot \mathbf{u})^2}{c_s^4} - \frac{\mathbf{u} \cdot \mathbf{u}}{2c_s^2} \right], & \alpha \neq 0 \end{cases},\quad (13)$$

where

$$\omega_\alpha = \begin{cases} 4/9, & \alpha = 0 \\ 1/9, & \alpha = 1, 3, 5, 7 \\ 1/36, & \alpha = 2, 4, 6, 8 \end{cases} \quad \text{for D2Q9 structure, (14a)}$$

$$\omega_\alpha = \begin{cases} 2/9, & \alpha = 0 \\ 1/9, & \alpha = 1, \dots, 6 \\ 1/72, & \alpha = 7, \dots, 14 \end{cases} \quad \text{for the D3Q15 structure.} \quad (14b)$$

In Eq. (13), c_s is the sound speed for an ideal fluid; for the D2Q9 and D3Q15 structures, $c_s = c/\sqrt{3}$.

We define the distribution function for the total force as

$$F_\alpha = \omega_\alpha (\mathbf{e}_\alpha / c_s^2) \cdot \mathbf{F} / \rho, \quad (15)$$

where the force \mathbf{F} is given by

$$\mathbf{F} = \mathbf{F}_s + \mathbf{F}_b + \mathbf{F}_p + \mathbf{F}_\mu. \quad (16)$$

In addition to the surface tension force \mathbf{F}_s and the physical body force \mathbf{F}_b in Eq. (8b), two further body-type forces, \mathbf{F}_p and \mathbf{F}_μ , are introduced associated with the pressure and the viscosity stress, respectively, to ensure that the lattice Boltzmann equation (10) exactly recovers the macroscopic momentum equation (8b). These forces are defined as

$$\mathbf{F}_p = -p \nabla \rho; \quad \mathbf{F}_\mu = [(\tau_f - 1/2)c_s^2 \delta t] (\nabla \mathbf{u} + \mathbf{u} \nabla) \cdot \nabla \rho. \quad (17)$$

The macroscopic quantities, \mathbf{u} and p can be evaluated as (see Appendix A)

$$\mathbf{u} = \sum_\alpha f_\alpha \mathbf{e}_\alpha + \frac{\mathbf{F}}{2\rho} \delta t, \quad (18a)$$

$$p = \left(\sum_{\alpha \neq 0} f_\alpha c_s^2 - \omega_0 |\mathbf{u}|^2 / 2 \right) / (1 - \omega_0). \quad (18b)$$

The dimensionless relaxation time τ_f is given by

$$\tau_f = \frac{\mu}{\rho c_s^2 \delta t} + \frac{1}{2}, \quad (19)$$

where the dynamic viscosity μ and the density ρ can be obtained from the distribution of phase field which will be given in Sec. II C.

In order to solve the coupled pressure and velocity in Eqs. (18a) and (18b), a prediction step is conducted first to provide the predicted pressure \hat{p} and velocity $\hat{\mathbf{u}}$ on the basis of the velocity at the previous time step, $\mathbf{u}^{t-\delta t}$,

$$\hat{p} = \left[\sum_{\alpha \neq 0} f_\alpha c_s^2 - \omega_0 |\mathbf{u}^{t-\delta t}|^2 / 2 \right] / (1 - \omega_0), \quad (20a)$$

$$\hat{\mathbf{u}} = \sum_\alpha f_\alpha \mathbf{e}_\alpha + \frac{\delta t}{2} [\mathbf{F}_s + \mathbf{F}_p(\hat{p}) + \mathbf{F}_\mu(\mathbf{u}^{t-\delta t}) + \mathbf{F}_b] / \rho. \quad (20b)$$

This is followed by a correction step,

$$p = \left(\sum_{\alpha \neq 0} f_\alpha c_s^2 - \omega_0 |\hat{\mathbf{u}}|^2 / 2 \right) / (1 - \omega_0), \quad (21a)$$

$$\mathbf{u} = \sum_\alpha f_\alpha \mathbf{e}_\alpha + \frac{\delta t}{2} [\mathbf{F}_s + \mathbf{F}_p(p) + \mathbf{F}_\mu(\hat{\mathbf{u}}) + \mathbf{F}_b] / \rho. \quad (21b)$$

The quantities used in the prediction step, including the square and derivatives of the velocities, can be taken from

intermediate results of the previous time step. Hence, the prediction step incurs only some additional local linear operations and, thus, the cost in computational time is small.

It will be shown that the new model can circumvent the inconsistency between the recovered momentum equations and the target momentum equations of incompressible multiphase flows (see Sec. III C). In addition, in comparison with existing models tested, the new model can better satisfy the divergence-free condition in the flow field and reduce the velocity fluctuations in high-pressure-gradient regions (see Sec. III E). As shown in Appendix A using a multiscaling expansion, the Navier-Stokes equations (8a) and (8b) can be precisely recovered by Eq. (10) to the order of $O(\delta t^2)$ for the continuity equation and $O(\delta t^2 + Ma^2 \delta t)$ for the momentum equation, where Ma denotes the Mach number.

C. LBE for interface capturing

The LBE for interface capturing is proposed to be in the following form:

$$\begin{aligned} g_\alpha(\mathbf{x} + \mathbf{e}_\alpha \delta t, t + \delta t) - g_\alpha(\mathbf{x}, t) \\ = -\frac{g_\alpha(\mathbf{x}, t) - g_\alpha^{\text{eq}}(\mathbf{x}, t)}{\tau_g} + \eta [g_\alpha^{\text{eq}}(\mathbf{x} + \mathbf{e}_\alpha \delta t, t) - g_\alpha^{\text{eq}}(\mathbf{x}, t)], \end{aligned} \quad (22)$$

where $g_\alpha(\mathbf{x}, t)$ is a distribution function for the order parameter ϕ , while $g_\alpha^{\text{eq}}(\mathbf{x}, t)$ is its corresponding equilibrium state; τ_g is a dimensionless relaxation time for the ϕ field; and η is a constant given by

$$\eta = 2\tau_g - 1. \quad (23)$$

Here, the basic form of the LBE for interface capturing is similar to that of Ref. [8], but there is a major difference in the last term. Unlike that in Ref. [8] where the term takes the form of $g_\alpha(\mathbf{x} + \mathbf{e}_\alpha \delta t, t) - g_\alpha(\mathbf{x}, t)$, which is used to produce the diffusion effects, the term in the present method is of its equilibrium state. This change allows the distribution function to approach an equilibrium state when the dimensionless relaxation time τ_g approaches unity, as shown in Eq. (22). This complies with the basic principles of the LB method. From a physical point of view, the particles away from equilibrium state are more likely to be unstable. By using this method, the stability of the interface between the two fluids predicted is significantly improved, as shown later.

We introduce the equilibrium distribution function g_α^{eq} as

$$g_\alpha^{\text{eq}} = \begin{cases} \phi - \frac{(1-\omega_0)\Gamma\mu_\phi}{(1-\eta)c_s^2}, & \alpha = 0 \\ \omega_\alpha \frac{\Gamma\mu_\phi + (\mathbf{e}_\alpha \cdot \mathbf{u})\phi}{(1-\eta)c_s^2}, & \alpha \neq 0 \end{cases} \quad (24)$$

so the moments of the equilibrium distribution function satisfy

$$\begin{aligned} \sum_\alpha g_\alpha^{\text{eq}} = \phi; \quad \sum_\alpha g_\alpha^{\text{eq}} \mathbf{e}_\alpha = \phi \mathbf{u} / (1 - \eta); \\ \sum_\alpha g_\alpha^{\text{eq}} \mathbf{e}_\alpha \mathbf{e}_\alpha = \Gamma \mu_\phi / (1 - \eta) \mathbf{I}, \end{aligned} \quad (25)$$

where Γ is a constant controlling the strength of mobility. In this model, the mobility is given by

$$M = (\tau_g - 1/2)\Gamma\delta t. \quad (26)$$

The order parameter ϕ can be calculated by

$$\phi = \sum_{\alpha} g_{\alpha}. \quad (27)$$

Then, according to mass conservation, the density ρ can be projected on the basis of ϕ as

$$\rho = \frac{\phi - \phi_B}{\phi_A - \phi_B} (\rho_A - \rho_B) + \rho_B. \quad (28)$$

In existing LBMs, the viscosity distribution in the interfacial region is given by either an exponential [41] or a linear [7,11,26] interpolation, namely

$$\mu = \mu_A^{\frac{\phi - \phi_B}{\phi_A - \phi_B}} \mu_B^{\frac{\phi_A - \phi}{\phi_A - \phi_B}} \quad (29a)$$

or

$$\mu = \frac{\phi - \phi_B}{\phi_A - \phi_B} (\mu_A - \mu_B) + \mu_B. \quad (29b)$$

Here, we propose a new expression for dynamic viscosity μ to ensure the continuity of viscosity flux across the interface, following that used in the conventional CFD method [42]. Consider a horizontal interface in a 2D x - y plane. Let u be the velocity in the horizontal direction, i.e., x direction; we note that the velocity gradient $\partial_y u$ is not necessarily continuous across the interface due to the difference in the fluid viscosities, but the viscosity flux $\mu \partial_y u$ is as required by the force balance. We define $(\partial_y u)_+$ and $(\partial_y u)_-$ as the velocity gradients on the two sides of the interface, and the corresponding values for viscosity are defined as μ_+ and μ_- , respectively. Since $\partial_y u$ is not continuous across the interface, we specify an averaged value of the $(\partial_y u)_+$ and $(\partial_y u)_-$ as the velocity gradient there, i.e., $\partial_y u = [(\partial_y u)_+ + (\partial_y u)_-]/2$. Then, due to the continuity of viscosity flux, we must have $\mu[(\partial_y u)_+ + (\partial_y u)_-]/2 = \mu_+(\partial_y u)_+ = \mu_-(\partial_y u)_-$. It is apparent that taking $1/\mu = (1/\mu_+ + 1/\mu_-)/2$ satisfies this requirement. The extension of this formula for an order parameter that continuously changes in the phase interfacial region is straightforward. The above expression implies that the mixture viscosity should be approximated using a linear interpolation, based on the order parameter, of the reciprocals of the viscosities, i.e., $1/\mu = (\phi - \phi_B)(1/\mu_A - 1/\mu_B)/(\phi_A - \phi_B) + 1/\mu_B$, rather than linearly interpolating the viscosity itself as Eq. (29b). Thus, we have

$$\mu = \frac{\mu_A \mu_B (\phi_A - \phi_B)}{(\phi - \phi_B) \mu_B + (\phi_A - \phi) \mu_A}. \quad (29c)$$

It is shown using multiscaling analysis (see Appendix B) that Eq. (9) can be recovered by the lattice Boltzmann equation (22) with an accuracy of $O(\delta t^2)$.

D. Discretizations

The first-order derivatives and the Laplacian of the force terms can be discretized using different schemes. It has been found in previous studies [27,43,44] that a discretization of the interfacial force with good isotropy can reduce the parasitic currents. Therefore, the following isotropic discretization is adopted:

$$\nabla \varphi = \sum_{\alpha \neq 0} \omega_{\alpha} \mathbf{e}_{\alpha} (\mathbf{e}_{\alpha} \cdot \nabla \varphi) / c_s^2, \quad (30a)$$

$$\nabla^2 \varphi = \sum_{\alpha \neq 0} \omega_{\alpha} (\mathbf{e}_{\alpha} \cdot \nabla)^2 \varphi / c_s^2, \quad (30b)$$

where φ is any macroscopic quantity. The second-order central difference is used to approximate the directional derivatives in \mathbf{e}_{α} direction as

$$\mathbf{e}_{\alpha} \cdot \nabla \varphi|_x = \frac{[\varphi(\mathbf{x} + \mathbf{e}_{\alpha} \delta t) - \varphi(\mathbf{x} - \mathbf{e}_{\alpha} \delta t)]}{2\delta t}, \quad (31a)$$

$$(\mathbf{e}_{\alpha} \cdot \nabla)^2 \varphi|_x = \frac{[\varphi(\mathbf{x} + \mathbf{e}_{\alpha} \delta t) - 2\varphi(\mathbf{x}) + \varphi(\mathbf{x} - \mathbf{e}_{\alpha} \delta t)]}{\delta t^2}. \quad (31b)$$

The scheme above is referred to as isotropic central scheme. An alternative is to follow the scheme of Lee and Fischer [43] to discretize \mathbf{F} in Eq. (15) with the isotropic central scheme and that in Eq. (18a) with the following isotropic mixed difference scheme:

$$\begin{aligned} \mathbf{e}_{\alpha} \cdot \nabla \varphi|_x \\ = \frac{[-\varphi(\mathbf{x} + 2\mathbf{e}_{\alpha} \delta t) + 5\varphi(\mathbf{x} + \mathbf{e}_{\alpha} \delta t) - 3\varphi(\mathbf{x}) - \varphi(\mathbf{x} - \mathbf{e}_{\alpha} \delta t)]}{4\delta t}. \end{aligned} \quad (32)$$

The above isotropic mixed difference scheme can provide a higher order isotropy and has shown the potential to further reduce the parasitic currents [43]. However, it does not conserve mass and momentum strictly due to the discretization errors [45]. In addition, its implementation is more complex and the efficiency may be lower since the force forms are discretized twice at each time step.

III. NUMERICAL TESTS

In this section, we test the performance of the proposed LBM model in terms of its accuracy and stability using a series of benchmark cases. Unless otherwise stated, we utilize the D2Q9 lattice structure for 2D problems and the D3Q15 lattice for 3D simulations and the first-order derivatives and the Laplacian equations are approximated with the isotropic central scheme [Eqs. (30) and (31)]. The treatments for boundaries used in the present numerical tests and some other commonly encountered boundaries are given in Appendix C.

A. Rigid-body rotation of Zalesak's disk

We first test the performance of the proposed boundary tracking method using a rigidly rotating Zalesak's disk [8,46]. Zalesak's disk is widely used for testing diffusion errors of an interface capturing method. As illustrated in Fig. 1, the disk studied has a slotted circular surface centred at $(0, 0)$ of a square computational domain with 200×200 lattice cells. The radius of the disk and the width of the slot occupy 80 and 15 lattice units, respectively. The disk rotates with a velocity field of a constant vorticity, $u_x = -U_0 \pi y/d$, $u_y = U_0 \pi x/d$, where $d = 200$ is the width of the computational domain and U_0 is a scale parameter which is kept at 0.02 in the present study. Theoretically, the disk should retain its shape during the rotation and complete one revolution every $T = 2d/U_0$ time units. This validation needs solving only the interface capturing equation, Eq. (22). The LBE for hydrodynamic properties is not needed, since the velocity is known. The interface thickness, surface

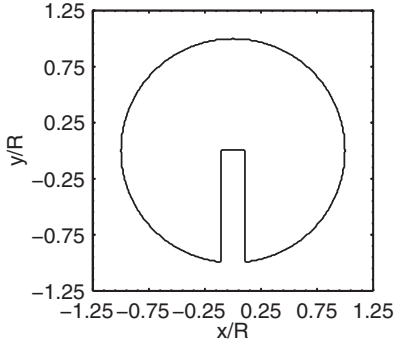
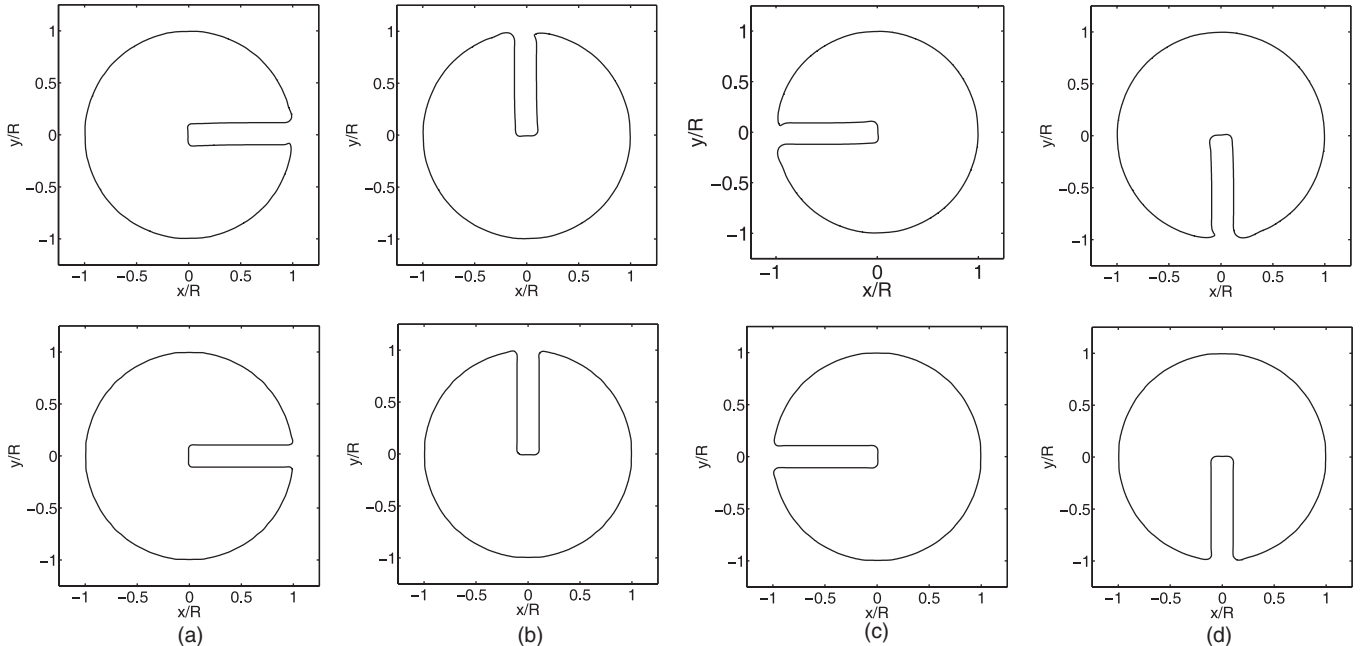


FIG. 1. Original shape and location of Zalesak's disk.

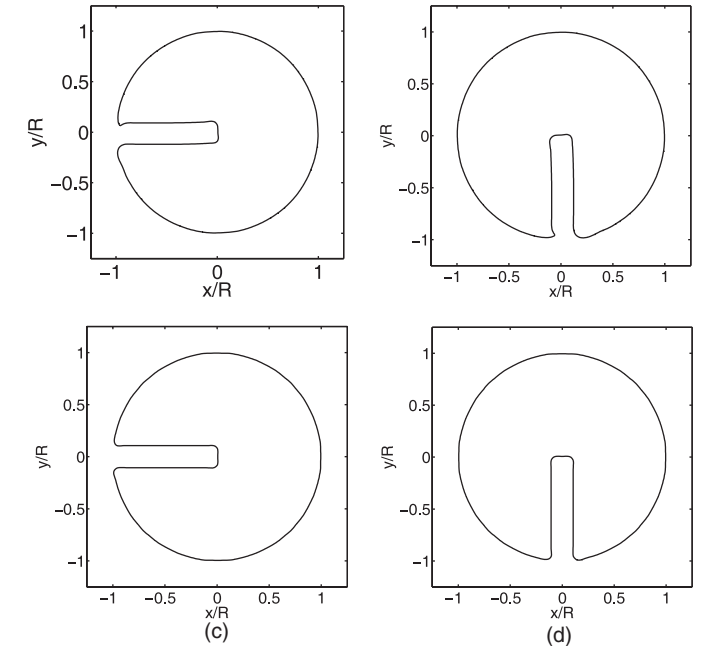
tension, order parameters, and relaxation time are $W = 2$, $\sigma = 0.04$, $\phi_A = -\phi_B = 1$, and $\tau_g = 0.75$, respectively. The Peclet number $\text{Pe} = U_0 W / [M\beta(\phi_A - \phi_B)^2]$ is introduced as the dimensionless mobility parameter. Two values of mobility, 0.01 and 0.003, are used for the current study so the corresponding Pe numbers are 200/3 and 2000/9, respectively. A periodic boundary condition is employed for all boundaries. The results obtained are compared with those of the LBM of Ref. [8]. As mentioned, the interface capturing method used here is similar to that of the method used in Ref. [8] but with a major alteration. To generate diffusion effects, the term of $g_\alpha(\mathbf{x} + \mathbf{e}_\alpha \delta t, t) - g_\alpha(\mathbf{x}, t)$ is used in Ref. [8], whereas in the present method, the spatial difference of the equilibrium state of the distribution function, i.e., $g_\alpha^{\text{eq}}(\mathbf{x} + \mathbf{e}_\alpha \delta t, t) - g_\alpha^{\text{eq}}(\mathbf{x}, t)$, is used. It is noted that the original model of Ref. [8] was applied on a D2Q5 lattice structure. However, we utilize the D2Q9 lattice here for both the present model and the model of Ref. [8] for comparison since the D2Q5 structure has some limitations. For example, there is no difference between the nonslip and free-slip boundary conditions in a D2Q5 lattice structure [11].

FIG. 2. Comparison of the evolution of the interface shape obtained by use of the present method (bottom) with that of the method in Ref. [8] (top), $\text{Pe} = 200/3$.

As shown in Fig. 2, for $\text{Pe} = 200/3$, both the current method and the method of Ref. [8] can produce a stable evolution of the interface. However, a close inspection shows that the slot of the disk is slightly twisted during the rotation in the results for the LBM of Ref. [8], whereas the current method tracks the interface more accurately with only a very small rounding of the sharp corners of the slot due to diffusion. The comparison for $\text{Pe} = 2000/9$ results is given in Fig. 3. For this larger Peclet number, the results for the LBM of Ref. [8] are unstable and the interface is jagged. In contrast, the present method can still capture the edge of the disk correctly albeit the sharp corners of the slot are twisted slightly [see Fig. 3(d)] as time goes on. Physically, the Peclet number gives the ratio of the convective velocity scale to the diffusive velocity scale. A large Peclet number implies that the convection effect is stronger than the diffusion effect. Thus, instability of the interface could potentially occur when the Peclet number is sufficiently large. This is the reason why Fakhari and Rahimian [11] found that their multi-relaxation-time LBM for interface capturing, which adopts the method of Ref. [8], was very sensitive to the mobility value.

B. Stationary droplet

A 2D stationary bubble or droplet is a major and demanding test to verify a model for multiphase flows, especially for the parasitic currents [11,28,43,45,47,48]. Here we simulate a 2D droplet in a stationary flow to further validate our LBM model. Initially, the circular droplet is placed in the middle of a computational domain of a 101×101 mesh. The radius of the droplet, R , occupies 25 lattice spacings. All the boundaries of the computational domain are set to be periodic. The model parameters are fixed as $\rho_A = 10$, $\rho_B = 1$, $\phi_A = 1$, $\phi_B = -1$, $\tau_f = 1$, $\tau_g = 0.8$, $W = 4$, and $\sigma = 0.002187$. To check the effects of mobility, three values, $M = 0.01, 0.1$ and 1 , are used



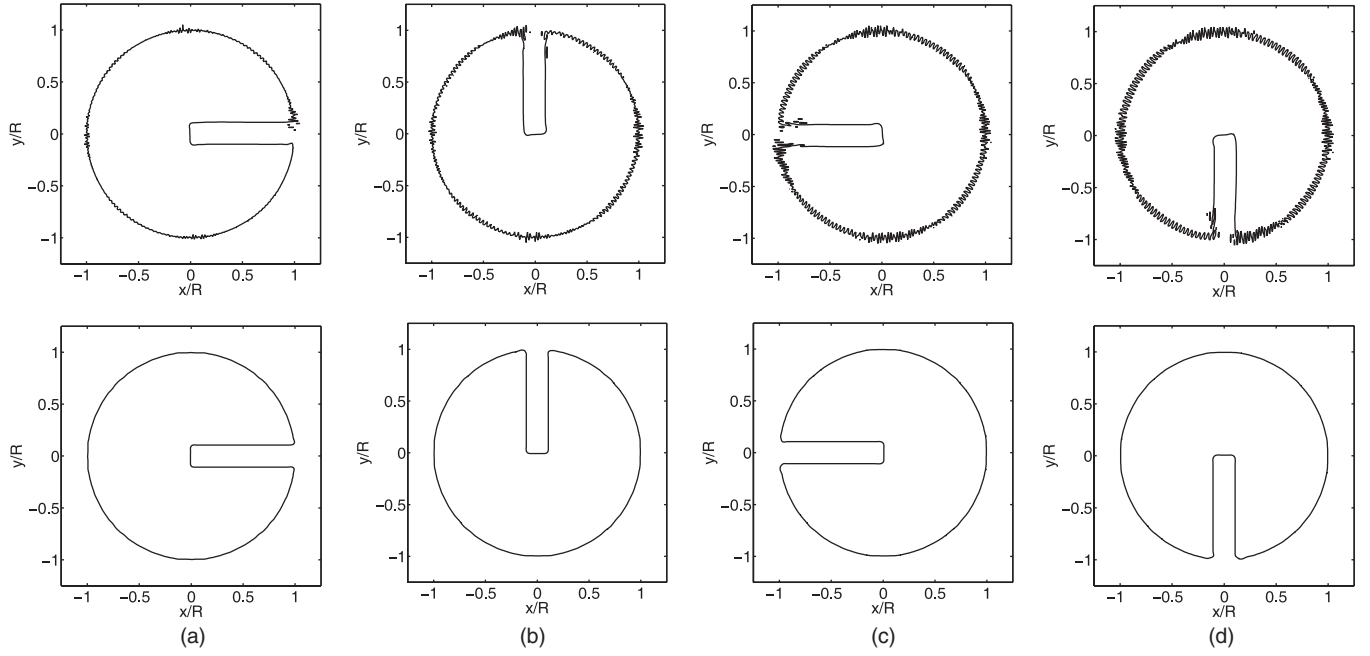


FIG. 3. Comparison of the evolution of the interface shape obtained by use of the present method (bottom) with that obtained by use of LBM in Ref. [8] (top), $\text{Pe} = 2000/9$.

for the tests. At the beginning of the simulation, the pressure of the whole system is set to be zero. According to the phase-field theory, the equilibrium distribution of the order parameter can be expressed as

$$\phi(x, y) = \frac{\phi_A + \phi_B}{2} + \frac{\phi_A - \phi_B}{2} \times \tanh\left(2 \frac{R - \sqrt{(x - x_c)^2 + (y - y_c)^2}}{W}\right), \quad (33a)$$

where x_c and y_c are the coordinates of the center of the droplet. Substituting the above expression into Eq. (28), we have

$$\rho(x, y) = \frac{\rho_A + \rho_B}{2} + \frac{\rho_A - \rho_B}{2} \times \tanh\left(2 \frac{R - \sqrt{(x - x_c)^2 + (y - y_c)^2}}{W}\right). \quad (33b)$$

The above two equations are used to generate the initial distribution of the order parameter and density, as well as used as the analytical solutions to verify the accuracy of the numerical results.

Figures 4(a)–4(c) show the velocity and momentum fields for $M = 0.01, 0.1$, and 1.0 , respectively, after 8×10^5 times of iteration. The solid line indicates the interface location, the arrowed lines are the streamlines of the flow fields, and the background of the figures is colorized with the momentum magnitude $\rho |\mathbf{u}|$. It can be clearly seen from the contours plot that higher momentum concentrates in the vicinity of the interface. It can also be seen from the streamlines that parasitic currents become increasingly evident with the increase of the mobility. In the cases of smaller values of mobility, $M = 0.01$ and 0.1 , unphysical velocity exists, which forms vortices around the interfaces, but the velocity in the direction normal to the interface is rather small. This is not the case for $M = 1.0$. The parasitic currents pass through the interface

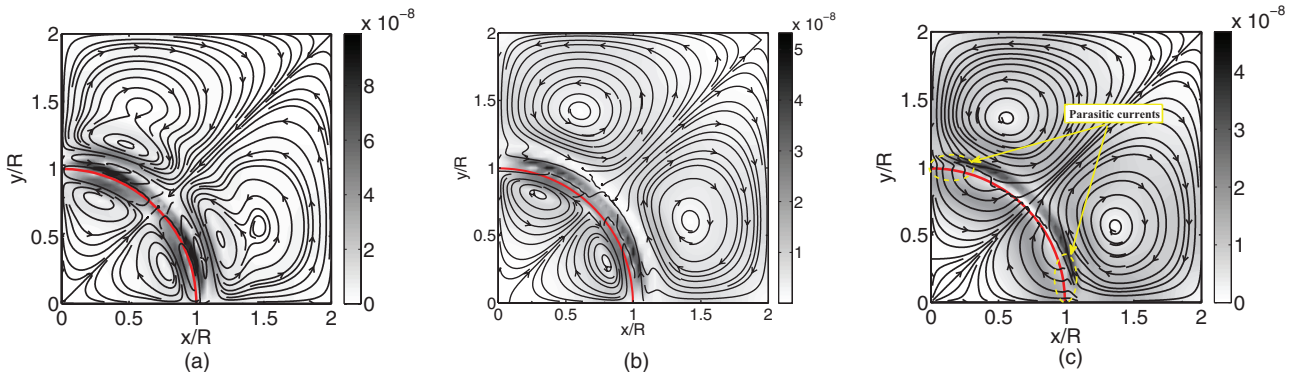


FIG. 4. (Color online) Velocity and momentum distributions at $t = 1 \times 10^6 \delta t$: (a) $M = 0.01$, (b) $M = 0.1$, (c) $M = 1.0$ (solid line: interface of two fluids; lines with arrow: streamlines; background color: momentum magnitude $\rho |\mathbf{u}|$).

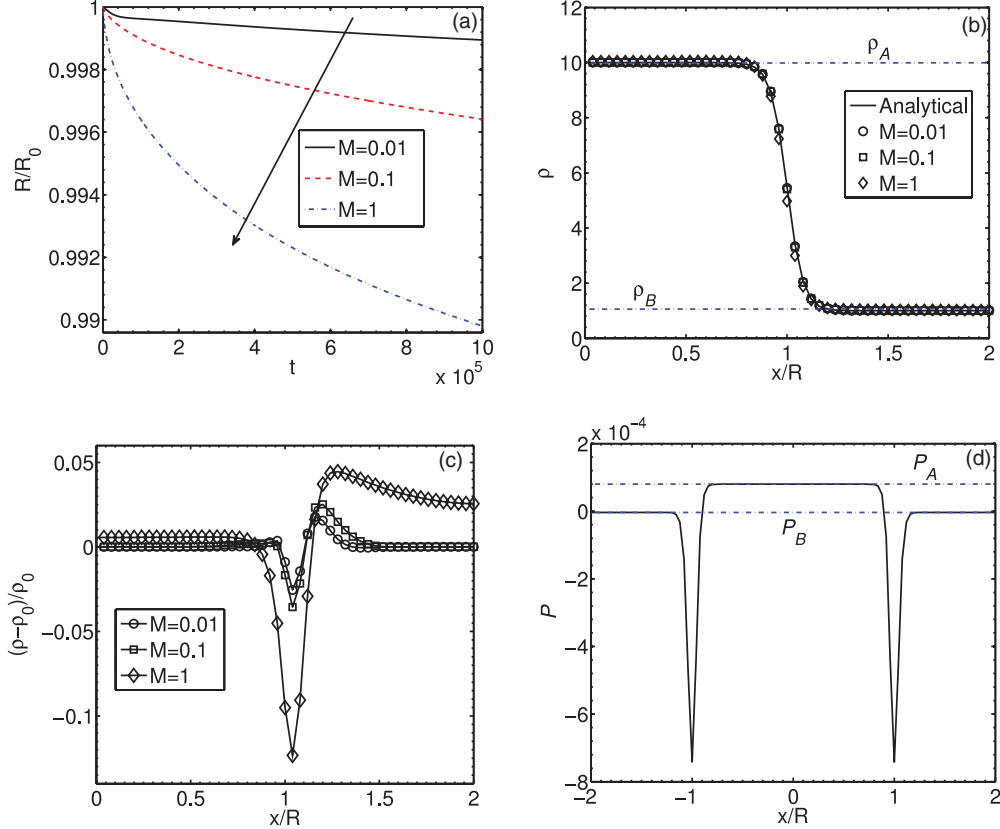


FIG. 5. (Color online) Time evolution of the radius over 1×10^6 times of iterations and the density and pressure profiles around the interface of a stationary droplet at $t = 1 \times 10^6 \delta t$. (a) Time evolution of dimensionless droplet radius; (b) density profile; (c) diffusion error; (d) pressure profile for $M = 0.01$.

can be observed clearly in Fig. 4(c) but not so clearly in Figs. 4(a) and 4(b). The presence of unphysical velocities and vortices around the interface are caused by the interfacial force applied. In addition, it is easy to see from the contours that, for $M = 0.01$, the momentum magnitude is largely symmetrical with respect to the interface of two fluids. However, this symmetry disappears with the increase of mobility due to the force imbalance in the vicinity of the interface.

The evolution of the droplet radius R nondimensionalized to the initial radius R_0 is plotted in Fig. 5(a) over a long time period of $1 \times 10^6 \delta t$ for cases of various values of mobility. The radius of the droplet decreases rapidly at the very early stage of the evolution and then reduces with a decreasing reduction rate. Moreover, the higher the value of the mobility, the higher the reduction rate. As a result, a larger mobility causes a bigger change in the droplet radius. It should be emphasized, however, that the change of the droplet radius, which is attributed to the parasitic currents across the surface of the droplet, is actually very small and is negligible for the cases of moderate values of mobility. After 1×10^6 times of iteration, the dimensionless droplet radius R/R_0 is 0.9989, 0.9964, and 0.9898 for $M = 0.01$, 0.1 and 1, respectively, which are at the same level of the parasitic currents in the model of Lee and Fischer [43], which gave a dimensionless droplet radius R/R_0 of 0.983 under a similar flow condition (noting that mobility is irrelevant in that model). This is a good demonstration of the improved performance of the present model in suppressing parasitic currents, as the model of Lee and Fischer [43] has

been known to be one of the best models in this regard, superior over many other LBMs, including, for example, the pseudopotential model of Shan and Chen [21] and the free energy model of Swift *et al.* [10,22]. The density profiles at $t = 1 \times 10^6 \delta t$ are shown in Fig. 5(b) as a function of the radial distance from the center of the droplet normalized by R . We observe that the density profiles match the analytical solution given by Eq. (33b) closely for the smaller values of mobility, $M = 0.01$ and 0.1, even after such a long time of iterations. For the case of $M = 1$, the model produces some visible errors. To further quantify the accuracy of the numerical results, we plot the relative errors of the predicted density profiles given by $(\rho - \rho_0)/\rho_0$ in Fig. 5(c), where ρ_0 is the analytical solution given by Eq. (33b). After 1×10^6 iterations, the maximum relative errors for $M = 0.01$, 0.1, and 1 are -2.55% , -3.55% , and -12.33% , respectively. For $M = 0.01$ and 0.1, the errors are not only small but also only concentrate in a narrow region across the interface. However, in the results of $M = 0.1$, larger errors appear in a wider region. It is noted that the mobility needs to be manipulated during the simulation to avoid numerical instability as mentioned in Sec. III A. We have found that, even for the case of a stationary droplet, a very small mobility may cause numerical instability, although the parasitic currents and diffusion errors can be reduced with decreasing mobility. For example, numerical instability occurs when the mobility is set to $M = 0.0001$ with all other parameters kept unchanged.

As mentioned above, the initial pressure of the whole system is zero. With correct pressure updating, even after a long time, the density profile should remain unchanged and the pressure jump across the interface, ΔP , should satisfy the Laplace law, i.e., $\Delta P = P_A - P_B = \sigma/R$, where, P_A and P_B are the pressure in the bulk fluids A and B, respectively. The pressure in our LBM is defined by $P = p_0 - k\phi\nabla^2\phi + k|\nabla\phi|^2/2 + p_h$, where, $p_0 = \phi\partial_\phi\psi - \psi$ is the equation of state of the system. For $M = 0.01$, Fig. 5(d) shows the pressure distribution in the radial direction at $t = 1 \times 10^6\delta t$. Similar pressure profiles can be obtained for the other two cases. The ratio between the surface tension calculated from pressure differences in fluids A and B, $\sigma_{\text{LBM}} = R\Delta P$, and the surface tension σ given by the analytical solution Eq. (6), i.e., $\sigma_{\text{LBM}}/\sigma$, are 0.9898, 0.9951, and 0.9951 for the cases of $M = 0.01$, 0.1, and 1.0, respectively. This good agreement demonstrates that the present LBM model can resolve the pressure field accurately.

C. Moving droplet

As mentioned before, one of the main objectives of the present study is to develop a phase-field-based LBM with the capability of simulating binary fluids with density differences. We now validate this capability of our LBM model. In many existing diffuse interface models [5,9,10,28,34,35], an average number density $n = (\rho_A + \rho_B)/2$ instead of the real fluid density ρ is used in the hydrodynamic equation. For an incompressible flow, the number density is uniform in the whole system and, therefore, the model is unable to simulate multiphase flows with density differences. In the present LBM, a real fluid density ρ is used in the LBE for the hydrodynamic properties so the N-S equation (8b) can be recovered. Thus, this model enables us to study the effects of the density ratio on the fluid flows. To verify this we carry out a simulation of a suddenly moved droplet [11]. As shown in Fig. 6, the droplet (fluid A) has a radius, R , occupying 15 lattice spacing and is surrounded by a quiescent gas phase (fluid B) in a rectangular computational domain of 181×121 lattice cells with free slip boundaries. At the beginning, the droplet is $2R$ away from the left boundary and is of the same distance to the upper and lower boundaries of the computational domain. The initial velocity field is given by $u_x = U_0(\phi - \phi_B)/(\phi_A - \phi_B)$, $u_y = 0$, where $U_0 = 0.1$ is the initial horizontal velocity in the bulk liquid phase. The parameters are chosen as $\tau_f = \tau_g = 0.8$, $W = 2$, $\sigma = 0.002$, $\rho_B = 1$, $\rho_A = 2$ and 5, $\phi_A = -\phi_B = (\rho_A - \rho_B)/2$, and $\text{Pe} = U_0 W/[M\beta(\phi_A - \phi_B)^2] = 500$. The dimensionless time is defined as $t^* = U_0 t/(2R)$. Physically, the droplet with a higher density should travel a longer distance than the less dense droplet for this particular case [11]. We first compare our results with those obtained by the binary fluid model in Ref. [28]. Figures 6(a) and 6(b) show the shape and location of the droplets with different densities at the same times of $t^* = 5$ and 10, respectively. The results of the present method are shown on the top and those of Ref. [28] at the bottom. As shown in the figure, the present model predicts that the droplet with a higher density travels further than that with a lower density, as expected. But the previous model [28] only predicts a very small effect of the density change.

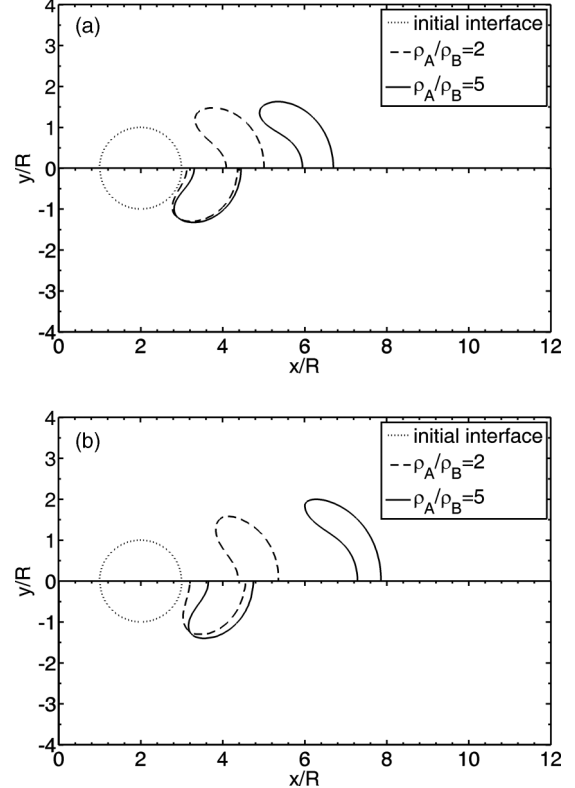


FIG. 6. Effects of density ratio on the droplet behaviors. Comparison of the present model (top) with the binary fluid model [28] (bottom). (a) $t^* = 5$; (b) $t^* = 10$.

To further check the reliability of the present model, we then compared our results with those of the index function model [26] which has the reputation to be able to correctly resolve droplet dynamics [27,49]. The comparisons of the evolution of the droplets with densities 2 and 5 are shown in Figs. 7(a) and 7(b), respectively. We can observe that the

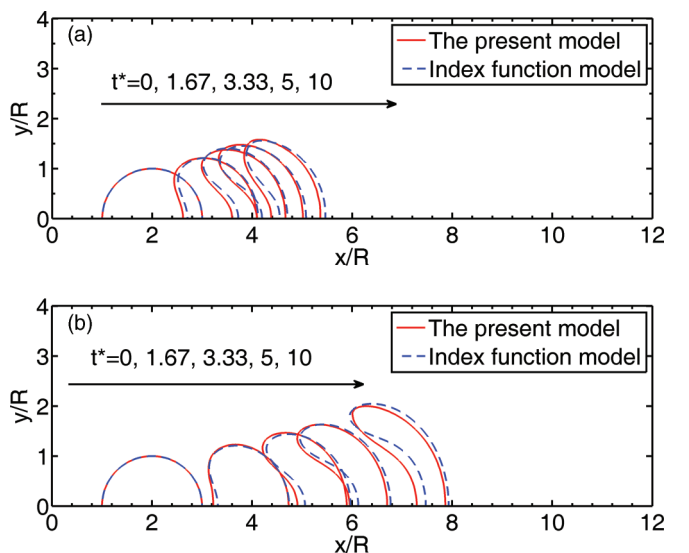


FIG. 7. (Color online) Effects of density ratio on the droplet behaviors. Comparison of the present model with the index function model [26]. (a) $\rho_A = 2$, $\rho_B = 1$; (b) $\rho_A = 5$, $\rho_B = 1$.

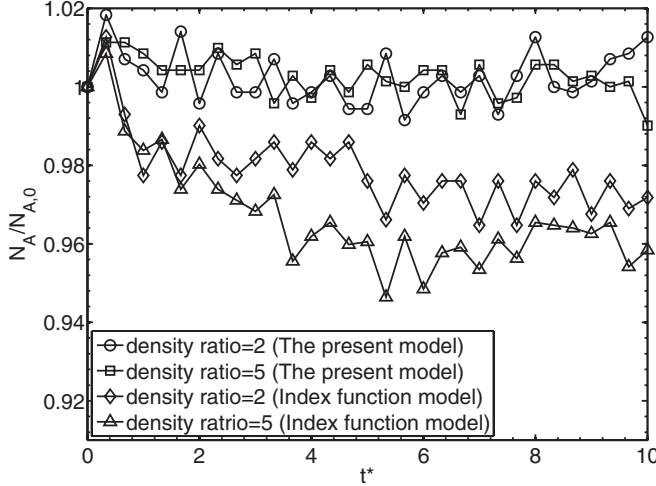


FIG. 8. Comparison of variations with time of droplet size obtained by use of the present model and the index function model [26].

droplet evaluations obtained by the two methods agree well, especially at the early stage of the droplet movement. As time goes on, small differences appear in both shape and location of the droplets. These differences are likely to be partly caused by the disagreement between the interfacial forces of the two models. The macroscopic momentum equation recovered by the index function model is $\partial_t(\rho\mathbf{u}) + \nabla \cdot (\rho\mathbf{u}\mathbf{u}) = -\nabla p_h + \nabla \cdot \Pi + \mathbf{F}_s + \mathbf{F}_b$. In comparison with the incompressible Navier-Stokes equation, Eq. (8b), there exists an artificial interfacial force $-\mathbf{u}[\partial_t\rho + \nabla \cdot (\rho\mathbf{u})]$ when the diffusion term in the Cahn-Hilliard equation is nonzero. In contrast, the present model truthfully recovers Eq. (8) and, hence, has no such artificial interfacial force. As pointed out in Ref. [33], with the increase of velocity or Reynolds number, this interfacial force will have an increasingly important influence on the interface and flow field. Similarly, the difference in the continuity equations recovered by the two models may also contribute to the differences in the numerical results, which will be discussed in more depth in the next section. Another reason for the differences in the numerical results is possibly due to the higher parasitic currents induced by the index function model. During the simulations, we observed that there were relative larger parasitic currents induced by the index function model, while the currents predicted by the present model are very small. To illustrate this, we plot the variation with time of dimensionless area of the droplet from the results of the two models in Fig. 8. For simplicity, we use the total number of grid points in the area where $\phi \geq 0$, referred to as N_A , as an indicator of droplet size, and define a dimensionless variable $N_A/N_{A,0}$, where $N_{A,0}$ is the initial value of N_A . The maximum change of the droplet size for density ratios of 2 and 5 are 1.78% and 1.29% in the simulations of the present model, whereas the corresponding changes induced by the index function model are 3.53% and 5.36%, respectively.

D. Spinodal decomposition

Spinodal decomposition [21,50–52], also referred to as separation of phases and components, is an important property of

mixtures of immiscible fluids. It occurs, for example, when one imposes initial compositional fluctuations on a homogeneous mixture in a metastable state. In this section, the separation of emulsified two fluids is simulated in 2D using the present model. This exercise focuses on the demonstration of the capability of the model in simulating components separation and, therefore, the physics of spinodal decomposition, such as the effects of the diffusion and convection and the power-law behavior of the domain-size growth [50–52], will not be discussed. We use a square domain with 151×151 nodes. Initially, the order-parameter distribution is treated as a small (1%) random perturbation around zero, and the velocity is zero in the whole domain. The model parameters are fixed as $W = 4$, $\sigma = 0.01$, $\phi_A = -\phi_B = 1$, $\rho_A = 10$, $\rho_B = 0.5$, $\tau_f = 1$, $\tau_g = 0.8$, and $M = 0.3$. Figure 9 shows the time evolution of the phase distribution, in which the phenomenon of fluid-fluid separation can be observed. Especially, as shown in Fig. 9(d), fluid B has separated from fluid A and formed some bubbles at $t = 25000 \delta t$. It is worth noting, however, that we failed to obtain the stable process of phase separation when the density ratio was increased to 100 ($\rho_A = 10$, $\rho_B = 0.1$). Although increasing the mobility can stabilize the flows for a longer period, the simulations would eventually become unstable.

E. 3D buoyancy-driven bubbly flow

As another test, a 3D buoyancy-driven bubbly flow is simulated to verify the accuracy of the present model in approximating the incompressible condition ($\nabla \cdot \mathbf{u} = 0$). To the best of our knowledge, all the existing LBM models for multiphase flow are momentum-based methods in which the equilibrium distribution functions are based on the fluid momentum $\rho\mathbf{u}$ [11,26,33] except a large-density-ratio model of Inamuro *et al.* [25], which is velocity based. In the model of Inamuro *et al.* [25], a velocity-correction is needed, which is performed iteratively by solving a Poisson equation of velocity and pressure. This costly procedure is conducted to enable the velocity to satisfy the divergence-free condition. In the present model, the velocity and pressure are solved explicitly with little cost. On the other hand, the continuity equation in momentum-based methods normally is in the form of $\partial_t p_h + \mathbf{u} \cdot \nabla p_h + \rho c_s^2 \nabla \cdot \mathbf{u} = 0$ [11,26,33]. In the low-frequency limit, the divergence-free condition of velocity is approximately satisfied when $\partial_t p_h \sim O(Ma^2)$ assuming $\mathbf{u} \cdot \nabla p_h$ is of the order of $O(Ma^3)$. In the present LBM, the divergence-free condition can be approximated with a higher accuracy of the order of $O(\delta t^2)$ (see Appendix A), namely the present model complies better with the divergence-free condition. This can be examined by comparing the results of the present model and the momentum-based methods. Here, the method of Li *et al.* [33], which is an improved version of Fakhari and Rahimian's model [11], is chosen for comparison. Li *et al.*'s method is chosen because it is one of the latest developments with good features such as recovering the Chan-Hilliard equation as well as having removed the artificial interface force $-\mathbf{u}[\partial_t\rho + \nabla \cdot (\rho\mathbf{u})]$ discussed in Sec. III C by adding $(\mathbf{u}M\nabla^2\mu_\phi)d_\phi\rho$ to the force term of LBE for hydrodynamic properties [33].

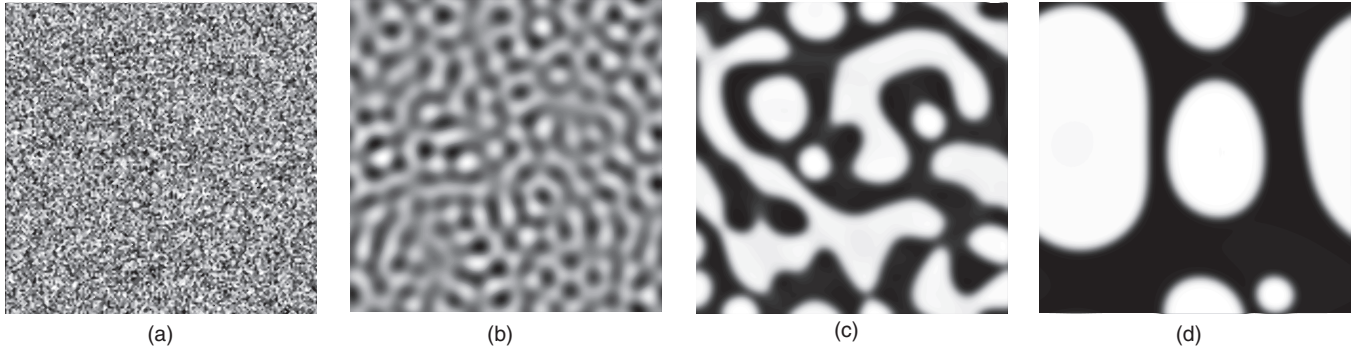


FIG. 9. Separation of binary fluid in 2D: distribution of order parameters at (a) $t = 0$, (b) $t = 5000\delta t$, (c) $t = 10000\delta t$, (d) $t = 25000\delta t$ shown in gray scale with the minimum in white and the maximum in black.

We consider the movement of a single bubble driven by the buoyancy. Initially, a spherical bubble (fluid B) without initial velocity is centered at $(0, 0, 0)$ of a cubic computational domain which is divided into $60 \times 60 \times 60$ cubic lattices. The radius of the initial bubble, R , occupies 15 lattice spaces. All the other spaces of the computational domain are occupied by a fluid with a higher density (fluid A) so the bubble is driven by the buoyancy force. To generate the buoyancy effects, a body force, $F_{b,z} = -(\rho - \rho_A)g$, is added to the vertical component of the force term of the momentum equation, where g is the gravitational acceleration. The common parameters used in the simulations with both of the models are $\rho_A = 20$, $\rho_B = 10$, $g = 1 \times 10^{-5}$, $M = 0.084$, $\tau_f = 0.8$, $W = 3$, $\sigma = 0.0022$, $\phi_A = -\phi_B = 0.5$. The periodic boundary condition is used on all the sides of the computational domain. The evolution of the bubble travelling velocity as a function of time is plotted in Fig. 10. Here, the bubble travelling velocity, \mathbf{u}_0 , is given by the volume average of the fluid velocity inside the bubble. As it is seen, the results obtained by the two different methods agree very well. The present method predicts a slightly higher velocity. This is likely to be caused by the difference in the continuity equations recovered by the two methods. To quantify this effect, the flow patterns around the bubble at $t = 3 \times 10^3\delta t$ and $t = 3 \times 10^4\delta t$ are shown in Figs. 11(a) and 11(b), respectively. The streamlines are based on the ralative velocity, $\mathbf{u}' = \mathbf{u} - \mathbf{u}_0$, and the backgrounds are

colored by the divergence of the velocity field. The results of the present LBM are shown on the left half, and those of the momentum-based method [33] are on the right. It can be clearly seen that the divergence of the velocity field is very small in the results of the present LBM, whereas relatively higher values of $\nabla \cdot \mathbf{u}$ appear in the simulations of the momentum-based method. The maximum values of $\nabla \cdot \mathbf{u}$ given by the present method are 2.72×10^{-7} and 1.79×10^{-6} at $t = 3 \times 10^3\delta t$ and $t = 3 \times 10^4\delta t$ repesctively; while the corresponding values in the results of the momentum-based method are 7.33×10^{-5} and 2.87×10^{-4} , respectively. As shown in the figures, the higher values of $\nabla \cdot \mathbf{u}$ predicted by the momentum-based method mostly concentrate in the vicinity of the head and tail of the bubble where a higher-pressure-gradient exists. Comparing the flow patterns obtained by the two different methods, we have found that there are observable differences in the velocity field in the regions where large $\nabla \cdot \mathbf{u}$ values appear in the results of the momentum-based method [33]. These differences become more and more evident with time. To track more closely the velocity field, we plot the velocity distributions along the center line of the bubble at $t = 3 \times 10^3\delta t$ and $t = 3 \times 10^4\delta t$, in Figs. 12(a) and 12(b), respectively. It can be seen that the momentum-based method induces velocity fluctuations around the interface of the two phases, which become stronger with time. Such velocity fluctuations may trigger numerical instability. We have found that when the density of the liquid phase is increased to $\rho_A = 100$, and all other parameters remain unchanged, the present method can still produce stable solution of bubble dynamics, whereas strong numerical instability occurs in the simulation of the momentum-based method, preventing a solution to be obtained.

The computational efficiency of the present model is comparable with those of four existing multicomponent LBM models. In these simulations, we have set the gravitational acceleration to zero, i.e. $\mathbf{F}_b = \mathbf{0}$, and keep all other parameters unchanged. The CPU times per time step by use of He *et al.*'s index function model [26], Zheng *et al.*'s density-matched model [28], Li *et al.*'s phase-field model [33], and the present model are 2.27 s, 1.66 s, 1.83 s, and 2.03 s, respectively, on a Core i7 3.4-GHz PC machine with 6 GB of RAM. Note that the computational efficiency of Zheng *et al.*'s model [28] has been compared with the chromodynamic model [20] and multicomponent pseudopotential model [21] in Ref. [53] for

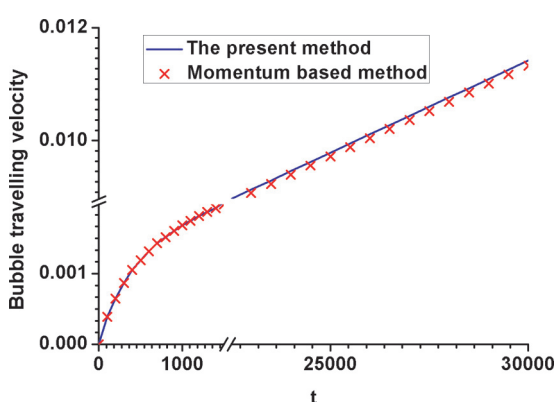


FIG. 10. (Color online) Variation with time of the bubble travelling velocity. Comparison of the present method and the momentum-based method of Li *et al.* [33].

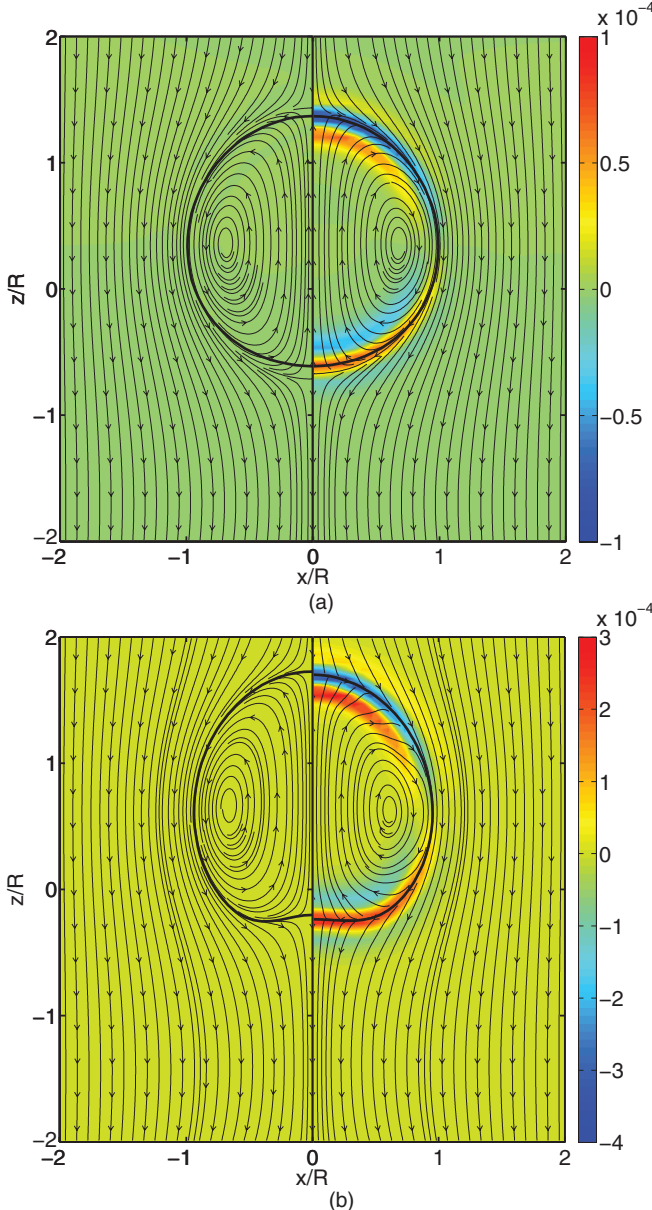


FIG. 11. (Color online) Flow field in the vertical middle cross section of the 3D bubble, Comparison of the present method (left half) with the momentum-based method [33] (right half): (a) $t = 3 \times 10^3 \delta t$ and (b) $t = 3 \times 10^4 \delta t$ (solid line: interface of two fluids; lines with arrow: streamlines; background color: divergence of the velocity filed $\nabla \cdot \mathbf{u}$).

multiphase flow in porous media. Combining the outcome of our comparison between the present model and Zheng *et al.*'s model [28] with that of the comparison in Ref. [53], it can be reasoned that the CPU time by the present model is likely to be about 1.36 and 1.07 times that of the chromodynamic model [20] and multicomponent pseudopotential model [21], respectively, when neglecting the difference between the model efficiency in boundary treatments.

F. Layered Poiseuille flow

The layered Poiseuille flow [54,55] between two infinite plates provides a good benchmark for validating the model's

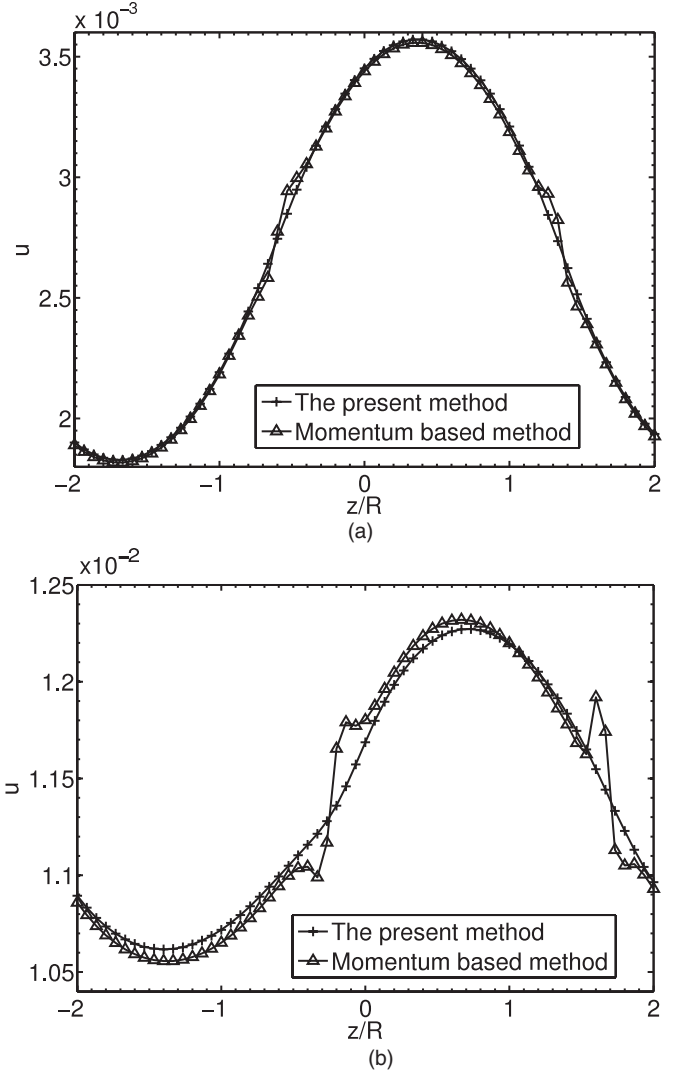


FIG. 12. Velocity distribution along the center line of the 3D bubble. Comparison of the present method and the momentum-based method of Li *et al.* [33]: (a) $t = 3 \times 10^3 \delta t$ and (b) $t = 3 \times 10^4 \delta t$.

capability to simulate binary fluids of different viscosities. Consider a channel flow of two incompressible immiscible fluids driven by a pressure gradient G in the x direction. The channel has an infinite length in the x direction and a width of $2h$ in the y direction. Initially, fluid A is located at the upper half of the channel ($0 < y \leq h$), while fluid B is at the bottom. ($-h \leq y < 0$). At the interface of the two fluids, the continuity of fluid velocity and stresses has to be satisfied. When the flow is sufficiently slow so no instabilities occur at the interface, an analytical solution with a steady velocity profile $u_{x,a}(y)$ exists,

$$u_{x,a}(y) = \begin{cases} \frac{Gh^2}{2\mu_A} \left[-\left(\frac{y}{h}\right)^2 - \frac{y}{h} \left(\frac{\mu_A - \mu_B}{\mu_B + \mu_A} \right) + \frac{2\mu_A}{\mu_A + \mu_B} \right], & 0 \leq y \leq h, \\ \frac{Gh^2}{2\mu_B} \left[-\left(\frac{y}{h}\right)^2 - \frac{y}{h} \left(\frac{\mu_A - \mu_B}{\mu_B + \mu_A} \right) + \frac{2\mu_B}{\mu_A + \mu_B} \right], & -h \leq y \leq 0. \end{cases} \quad (34)$$

Giving a pressure gradient of $G = u_c(\mu_A + \mu_B)/h^2$, the flow can achieve a steady velocity of u_c at the center.

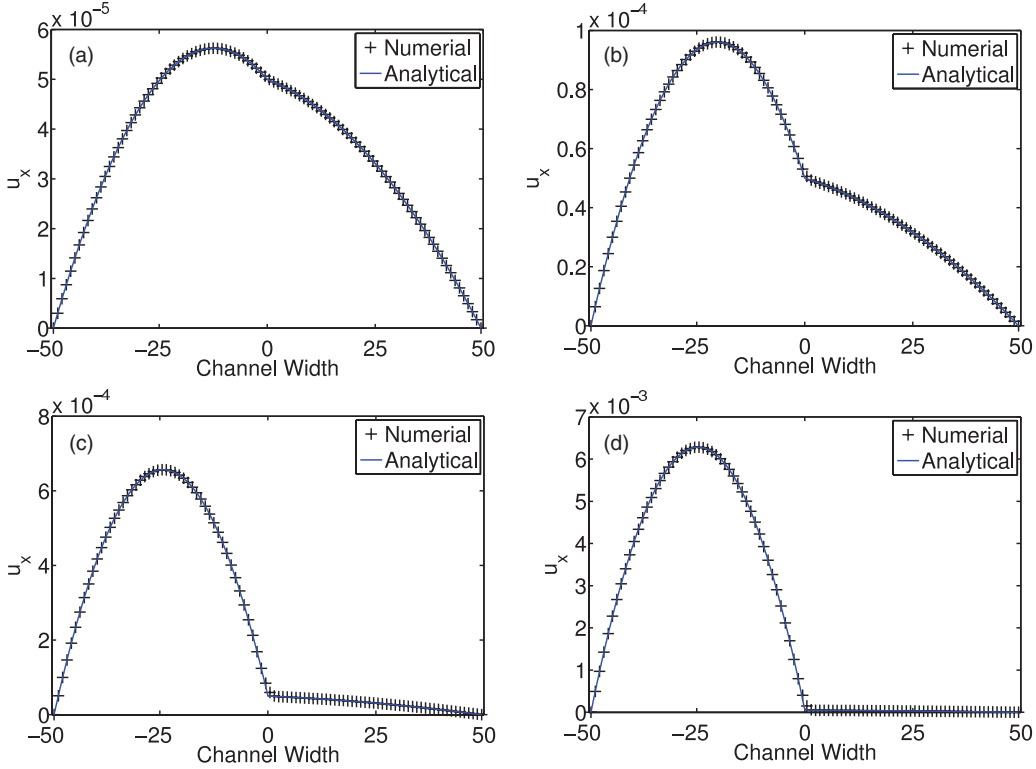


FIG. 13. (Color online) Comparison of the velocity profiles obtained by use of the present LBM with Viscosity I (+) with the analytical results (solid line): (a) $\mu_A/\mu_B = 3$; (b) $\mu_A/\mu_B = 10$; (c) $\mu_A/\mu_B = 100$; (d) $\mu_A/\mu_B = 1000$.

Simulations are conducted on a computational domain of 100×100 lattice cells and results are to be compared with the analytical solution. The periodic boundary condition is applied in the flow direction and the no-slip boundary condition is enforced on the upper and lower walls. The system is started from rest and a body force $F_{b,x} = u_c(\mu_A + \mu_B)/h^2$ is added to the x component of the force term to mimic the pressure gradient. It should be pointed out that artificially adding body force $F_{b,x}$ to mimic the pressure gradient G is not precisely valid in the presence of a density gradient, but it is not yet clear how to implement a consistent body force when a density contrast exists [55,56]. Thus, a binary fluid with a uniform density is considered here. A small value of $u_c = 5 \times 10^{-5}$ is chosen to ensure the stability of the interface to be maintained. Since the interface is planar, the curvature and surface tension forces are zero. Four different viscosity ratios of $\mu_A/\mu_B = 3, 10, 100$, and 1000 are used in the simulations. Other parameters are fixed as $W = 4$, $\rho_A = \rho_B = 1$, $\phi_A = -\phi_B = 0.5$, $M = 0$. For simplicity, we refer to the newly proposed interpolation method for the viscosity distribution, i.e., Eq. (29c), as Viscosity I, and the methods given by Eqs. (29a) and (29b) as Viscosity II and Viscosity III, respectively. Figures 13(a)–13(d) show the numerical solutions of the present LBM with Viscosity I and corresponding analytical solutions for viscosity ratios of 3, 10, 100, and 1000, respectively. We see a very good agreement between the numerical predictions and the analytical solutions even for a large viscosity ratio of 1000. Figure 14(a) shows a comparison of the predicted velocity profiles using the different mixture viscosity models for $\mu_A/\mu_B = 100$. It can be observed that the results of Viscosity I agree with the analytical solution very

well, whereas the results of Viscosity II and III show obvious discrepancies with the analytical solution, although Viscosity II is significantly better than Viscosity III. To further check the

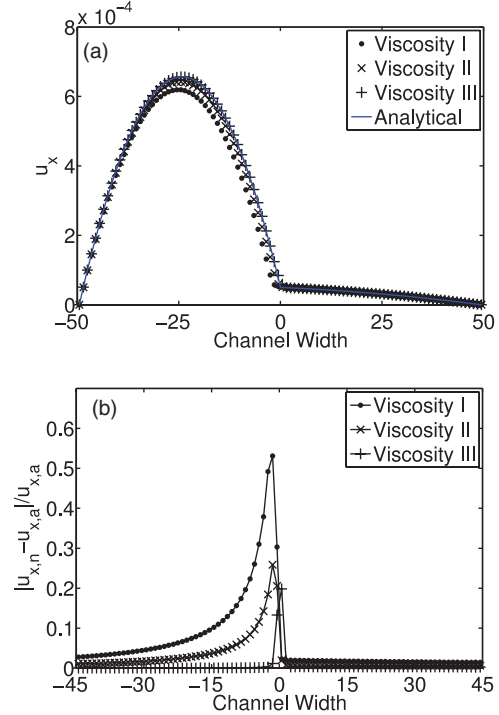


FIG. 14. (Color online) Comparison of the numerical results of the different mixture viscosities for $\mu_A/\mu_B = 100$: (a) velocity profiles and (b) relative errors.

TABLE I. Relative errors (%) in the velocity profile at different positions for the layered Poiseuille flow; (I) Viscosity I; (II) Viscosity II; (III) Viscosity III.

y	$\mu_A/\mu_B = 10$			$\mu_A/\mu_B = 100$			$\mu_A/\mu_B = 1000$		
	(I) (%)	(II) (%)	(III) (%)	(I) (%)	(II) (%)	(III) (%)	(I) (%)	(II) (%)	(III) (%)
-37.5	0.03	0.73	1.47	0.02	1.34	3.42	0.02	2.42	1.99
-25.5	0.03	1.00	2.00	0.03	2.09	5.45	0.03	3.78	4.72
-12.5	0.04	1.62	3.23	0.06	4.48	11.89	0.07	8.34	11.58
-5.5	0.06	2.41	4.81	0.13	9.74	26.04	0.16	19.61	33.8
5.5	0.02	0.38	0.75	0.33	0.77	1.92	1.30	2.18	4.33
12.5	0.02	0.36	0.70	0.33	0.72	1.80	2.03	2.13	3.95
25.5	0.01	0.33	0.63	0.31	0.65	1.63	1.92	2.39	3.02
37.5	0.02	0.32	0.60	0.28	0.62	1.52	0.85	3.33	1.59

effects of the viscosity scheme on the numerical accuracy, the relative errors of the evaluated velocity profiles obtained by the different viscosity schemes are plotted in Fig. 14(b). Here, the relative error is defined as the absolute value of the discrepancy between the numerical velocity $u_{x,n}$ and analytical velocity $u_{x,a}$ divided by the analytical solution $u_{x,a}$. From Fig. 14(b), it can be seen that not only Viscosity I produces a smaller error, but also the region where any error occurs is much narrower. This error stems from the diffused thickness of the interface. In the analytical solution, $\partial_y u$ has a step change across the interface, whereas it is diffused in the numerical solution. In the results of Viscosity II and Viscosity III, larger errors appear in a wider region, concentrating on the less viscous side of the interface. For the different viscosity ratios, a quantitative comparison of the relative errors at different positions in the y direction can be found in Table I. For the low viscosity ratio of $\mu_A/\mu_B = 10$, all the three viscosity schemes can give acceptable accuracy. However, Viscosity II and Viscosity III become less accurate with an increasing viscosity ratio.

G. Rayleigh-Taylor instability

To further demonstrate the accuracy of the present model in solving more complicated flows, we carry out a simulation of the Rayleigh-Taylor instability, which occurs if any perturbation is caused along the interface between a heavier fluid A on top of a lighter fluid B fluid in a gravitational field. This is a classical problem that has been investigated by many numerical methods [7,16,26,33,57–61].

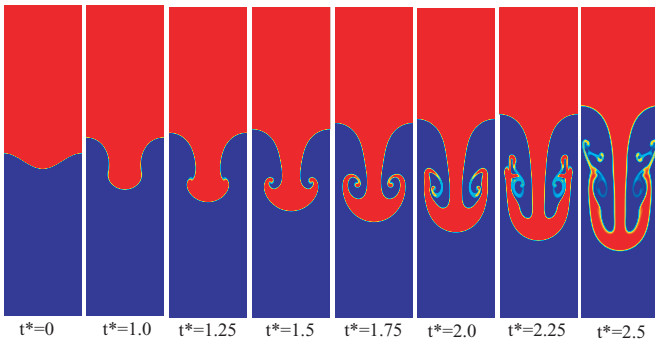


FIG. 15. (Color online) Evolution of the interface patterns of the 2D Rayleigh-Taylor instability.

We first simulate a typical case of a 2D Rayleigh-Taylor instability in the viscous regime. Consider two layers of the fluids with zero surface tension initially at rest in the gravity field in a domain of $[-d/2, d/2] \times [-2d, 2d]$. The initial interface

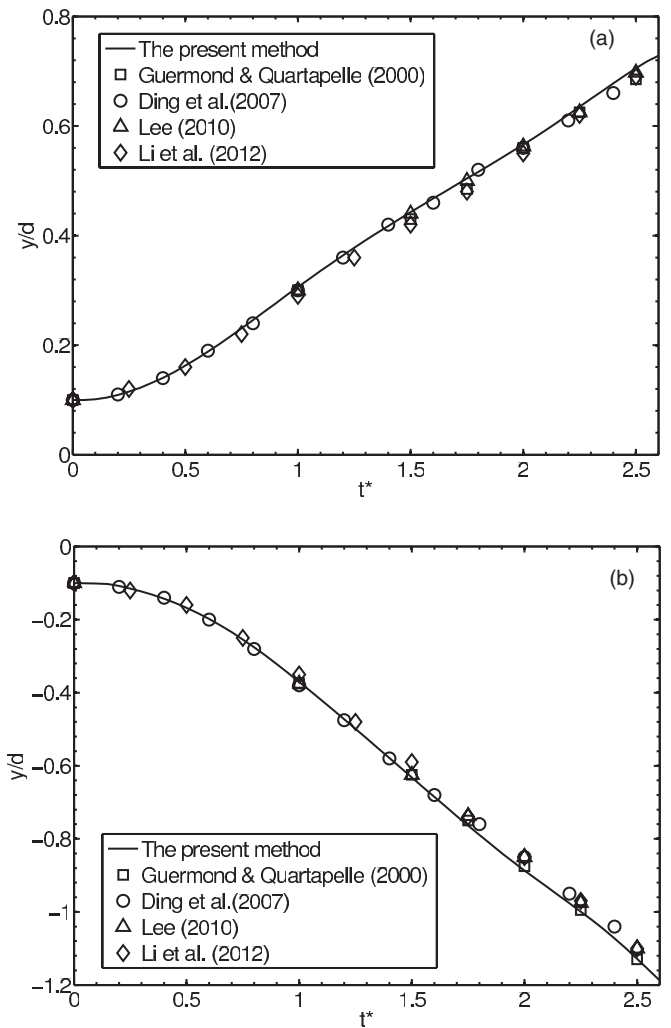


FIG. 16. Variation with time of the positions of the bubble front and spike tip. Comparison with the results of Qin *et al.* [7], Guermond and Quartapelle [58], Lee [59], and Li *et al.* [33]. (a) Bubble and (b) spike.

position of the two fluids is $H(x) = 0.1d \cos(2\pi x/d)$. Due to the instability of the interface, the heavy and light fluids will penetrate into each other with time. To enable a comparison between the present results and available data reported in the literature [7,33,58,59], we use an Atwood number of $A_t = (\rho_A - \rho_B)/(\rho_A + \rho_B) = 0.5$ and a Reynolds number of $\text{Re} = \rho_A d^{3/2} g^{1/2}/\mu = 3000$, where g is the gravitational acceleration pointing downward. The dimensionless time and mobility parameters are defined as $t^* = t/\sqrt{d/(gA_t)}$ and $\text{Pe} = \sqrt{gd} W/[M\beta(\phi_A - \phi_B)^2]$. The simulation is carried out on a 200×800 grid, i.e., $d = 200$. The interface width and Peclet number are set to be $W = 5$, $\text{Pe} = 105$, respectively. The no-slip condition is imposed at the top and bottom walls while the periodic boundary condition is applied on the two vertical sides. Figure 15 depicts the interface pattern at dimensionless times $t^* = 0, 1, 1.25, 1.5, 1.75, 2, 2.25$, and 2.5 . It can be seen that, due to the effects of gravity, the fingers of lighter fluid, referred to as “bubbles,” penetrate into the heavier fluid; while the “spike” of the heavier fluid falls into the lighter fluid with a rolling-up process. At the early stage, the heavy fluid rolls up into two counter-rotating vortices along the sides of the spike. As time goes on, the vortices grow in size and ultimately are shed into the wake, forming a pair of secondary vortices which appear at the tails of the roll-ups. The flow patterns obtained by the present study, not only the global characteristics of the flow but also the detailed vortex structures, agree very well with those in Ref. [7]. As a further check on the consistency of the present numerical results and those reported in the literature, the positions of the bubble front and spike tip as a function of time are plotted in Figs. 16(a) and 16(b), respectively. Some representative points taken from the studies of Qin *et al.* [7], Guermond and Quartapelle [58], Lee [59], and Li *et al.* [33] are shown in the figures to illustrate the degree of the quantitative agreement. The minor discrepancy may be due to the differences in the temporal and spatial resolutions,

the interface width, and Peclet number used in the different studies since the effects of model formulations are likely to be small because of the zero surface tension, the low density ratio, and the same dynamic viscosity of the two fluids used in the two simulations.

Next, in the same manner as in Ref. [16], a simulation of a 3D Rayleigh-Taylor is performed to verify the model’s ability to predict complicated flows in 3D. Consider two layers of fluids of the same kinetic viscosity, ν , in a rectangular box with a square horizontal cross section and a height-width aspect ratio of 4:1. The domain is $[-d/2, d/2] \times [-d/2, d/2] \times [-2d, 2d]$, and the initial position of the interface is $H(x, y) = 0.05d[\cos(2\pi x/d) + \cos(2\pi y/d)]$. The Atwood number is set to be 0.5. To be consistent with the study of Ref. [16], the Reynolds number is chosen as $\text{Re} = d^{3/2} g^{1/2}/\nu = 128$. The dimensionless time is defined as $t' = t/\sqrt{d/g}$. The simulation is performed on a $64 \times 64 \times 256$ grid, i.e., $d = 64$. The interface width and Peclet number are set to be $W = 5$, $\text{Pe} = 744$, respectively. The evolution of the interface is shown in Fig. 17 at dimensionless times $t' = 1, 2, 3, 4$, and 4.5 . As is expected, the heavy and light fluids penetrate into each other to form the spike and bubbles under the action of gravity. At the early stage, the evaluation of the interface shape is rather simple. As time goes on, the roll-ups of the falling fluid appear. The first roll-up appears in the vicinity of the saddle points, followed by the occurrence of the mushroomlike roll-up along the flank of the spike. The definition of the saddle point can be found in Fig. 17(a). The interfacial patterns obtained in this work appear to compare well with those in Ref. [16]. A quantitative comparison of the variations with times of the positions of the bubble front, saddle point, and spike tip obtained by the present study and the study in Ref. [16] is given in Fig. 18, which shows an excellent agreement between the results from these studies. This is good evidence of the capability of the new model in dealing with complex two-phase

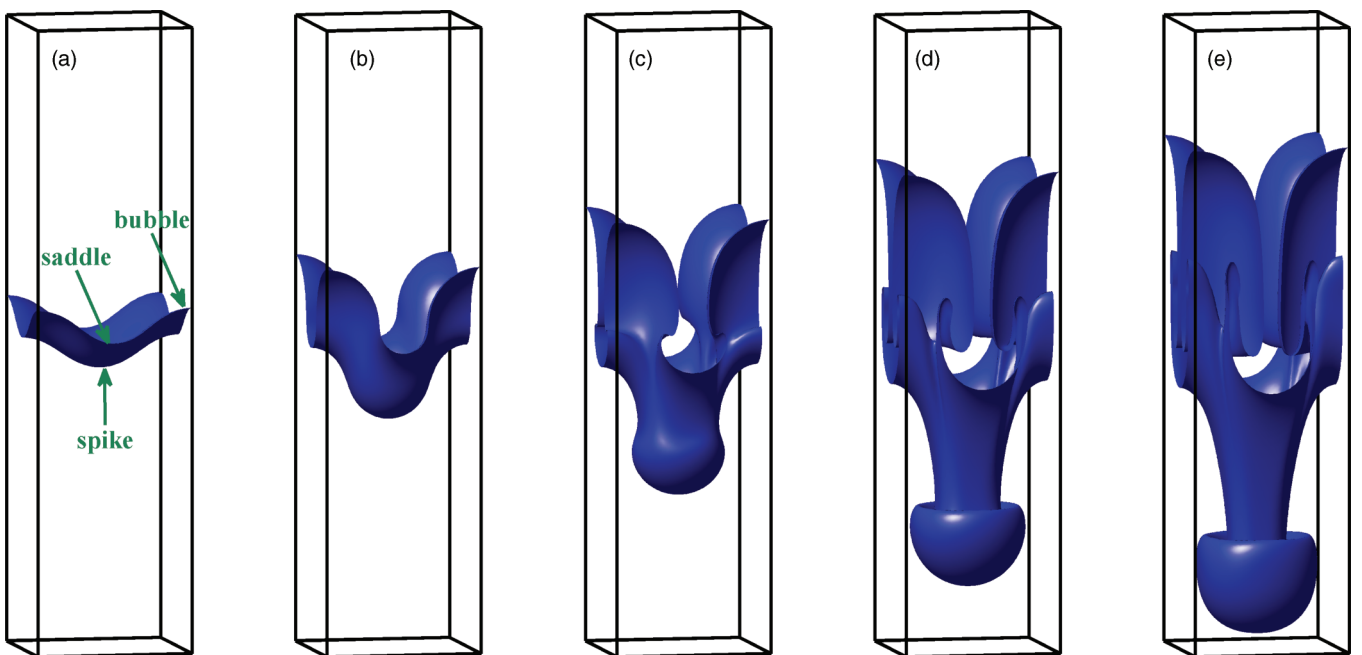


FIG. 17. (Color online) Evolution of the interface patterns of the 3D Rayleigh-Taylor instability.

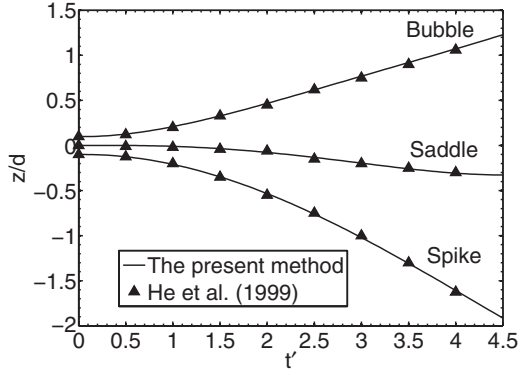


FIG. 18. Variation with time of the positions of the bubble front, saddle point, and spike tip. Comparison with the results of He *et al.* [16].

flows as the numerical simulations of Ref. [16], which is based on the index function model of He *et al.* [26], are known to be of high accuracy for this particular problem. The potential weakness of the index function model [26] in the area of parasitic currents does not show up due to the zero surface tension and small density ratio used in this test. Furthermore, the issues of the potentially weak divergence-free condition and the artificial interfacial force in the index function model have insignificant consequences in this test case due to low local velocities around the interface of the two fluids [33].

IV. CONCLUSIONS

In this study, a LBM model is proposed based on the phase-field theory to simulate incompressible binary fluids with density and viscosity contrasts. The new model aims at improving the performance of LBM modelling of binary fluids in terms of (i) improving the accuracy and stability of interface tracking, (ii) achieving consistency between the LBEs and the target macroscopic equations to faithfully reflect the incompressible fluid condition through the introduction of a velocity-based LBE scheme, and (iii) better capability and accuracy in dealing with binary fluids with density and viscosity differences. Two LBEs are utilized in the new model: one for the interface capturing and the other for solving hydrodynamic properties. A multiscaling analysis shows that the LBE for interface capturing can precisely recover the Chan-Hilliard equation with an accuracy of $O(\delta t^2)$, while the LBE for the hydrodynamic properties can recover the incompressible Navier-Stokes equation given by the phase-field theory to an order of $O(\delta t^2)$ for the continuity equation and $O(\delta t^2 + Ma^2 \delta t)$ for the momentum equation. Unlike many existing LBM models for binary fluids which are limited to density matched fluids, the proposed model is capable of dealing with binary fluids with moderate density ratios by using the real fluid density rather than the average number density in the LBE for the hydrodynamic properties. In addition, a new projection scheme for the mixture viscosity is introduced to model binary fluids with viscosity contrasts.

The method reflects the continuity of viscosity flux across the interface.

In order to validate the performance of the proposed model, a series of 2D and 3D benchmark problems have been solved, which include rigid-body rotation of a Zalesak's disk, stationary and moving droplets, spinodal decomposition, buoyancy-driven bubbly flow, layered Poiseuille flow, and the Rayleigh-Taylor instability. The results compare well with analytical solutions and/or classic numerical predictions. Moreover, it is found that the proposed model can track the interface of two-phase flows more accurately and stably than the existing methods tested and is able to systematically remove or reduce the parasitic current across the interface. It has been shown that the newly developed velocity-based model produces much less artificial velocity around the interfaces than momentum-based models, achieving a better agreement with the incompressible fluid condition. Moreover, the present model can eliminate or reduce the velocity fluctuations in high-pressure-gradient regions, achieving a better numerical stability in comparison with the momentum-based models. In addition, the test of the layered Poiseuille flow shows that the proposed method for the projection from phase field to viscosity field performs significantly better than the traditional schemes of mixture viscosity such as linear and exponential interpolations.

A limitation of the present model is the introduction of velocity derivatives into the interfacial force term, which is usually not necessary in the existing models for binary fluids with moderate density ratios. This reduces the locality of the algorithm, leading to a reduction in the efficiency of the parallel implementation to some extent. In addition, due to the absence of an H theorem, the present model does not guarantee an unconditional stability. More specifically, we can provide the following guidelines on the parametric domain within which our new model is applicable. First, the flow velocity should be much smaller than the sound speed c_s to satisfy the incompressible limit. With the increase of the local flow velocity, the fluctuation of the hydrodynamic pressure, which is of the second order of Mach number under incompressible limit, may be amplified, causing instability. In the present model, the critical velocity is up to 0.1. Second, the viscosity ratio should also be below a critical value, which is a function of parameters such as the density ratio and relaxation time $\tau_f (> 0.5$ for positive kinetic viscosity). The critical ratio is also influenced by the grid size. Our numerical experiments show that the present LBM can remain stable when the viscosity ratio is as high as 1000 for some cases. The critical surface tension in the present model can be up to 0.05, or even higher, by manipulating the mobility parameters to control the level of diffusion effects. Finally, we note that the present model is more susceptible to numerical instability at high density ratios when the gradient of velocity or pressure field is high. For example, the critical density ratio is restricted to about 10 only when the flow velocity is 0.1. With a lower flow velocity, a higher density ratio can be achieved. Several approaches are available which can be adopted to overcome the limitation on the density ratio, including, for example, incorporating a nonuniform mobility into the Chan-Hilliard equation, implementing a filtering operation to the pressure field, or utilizing more stable discretization schemes, all of which are beyond the scope of the present paper.

ACKNOWLEDGMENTS

This work is supported by the Engineering and Physical Sciences Research Council of the United Kingdom under Grant No. EP/I010971/1.

APPENDIX A: MULTISCALE ANALYSIS OF LBE FOR HYDRODYNAMIC PROPERTIES

To obtain the macrodynamic behavior arising from the lattice Boltzmann equation (10), a multiscaling analysis is performed by introducing the following expansions:

$$f_\alpha = f_\alpha^{(0)}(\mathbf{x}, t) + \varepsilon f_\alpha^{(1)}(\mathbf{x}, t) + \varepsilon^2 f_\alpha^{(2)}(\mathbf{x}, t), \quad (\text{A1})$$

$$\partial_t = \varepsilon \partial_{t1} + \varepsilon^2 \partial_{t2}; \quad \nabla = \varepsilon \nabla_1; \quad F_\alpha = \varepsilon F_{\alpha 1}, \quad (\text{A2})$$

where ε is an expansion parameter which is proportional to the ratio of the lattice spacing to a characteristic macroscopic length [39,56,62].

Using the Taylor series expansion to the second order, Eq. (10) can be rewritten as

$$\begin{aligned} & \left[\delta t (\partial_t + \mathbf{e}_\alpha \cdot \nabla) + \frac{\delta t^2}{2} (\partial_t + \mathbf{e}_\alpha \cdot \nabla)^2 \right] f_\alpha \\ &= -\frac{f_\alpha(\mathbf{x}, t) - f_\alpha^{\text{eq}}(\mathbf{x}, t)}{\tau_f} + \frac{2\tau_f - 1}{2\tau_f} F_\alpha \delta t + O(\delta t^3). \end{aligned} \quad (\text{A3})$$

Substituting Eqs. (A1) and (A2) into Eq. (A3), the infinite consecutive series of equations (Chapman-Enskog system) can be obtained:

$$O(\varepsilon^0): f_\alpha^{(0)} = f_\alpha^{\text{eq}} + O(\delta t^3), \quad (\text{A4})$$

$$O(\varepsilon^1): \delta t [\partial_{t1} + \mathbf{e}_\alpha \cdot \nabla_1] f_\alpha^{(0)} = -\frac{f_\alpha^{(1)}}{\tau_f} + \frac{2\tau_f - 1}{2\tau_f} F_{\alpha 1} \delta t, \quad (\text{A5})$$

$$\begin{aligned} O(\varepsilon^2): & \delta t [\partial_{t2} f_\alpha^{(0)} + (\partial_{t1} + \mathbf{e}_\alpha \cdot \nabla_1) f_\alpha^{(1)}] \\ &+ \frac{\delta t^2}{2} [(\partial_{t1} + \mathbf{e}_\alpha \cdot \nabla_1)^2] f_\alpha^{(0)} = -\frac{f_\alpha^{(2)}}{\tau_f}. \end{aligned} \quad (\text{A6})$$

Then, the substitution of Eq. (A5) into Eq. (A6) yields

$$\begin{aligned} & \delta t \partial_{t2} f_\alpha^{(0)} + \delta t^2 \{ (1/2 - \tau_f) (\partial_{t1} + \mathbf{e}_\alpha \cdot \nabla_1)^2 f_\alpha^{(0)} \\ & - [(\partial_{t1} + \mathbf{e}_\alpha \cdot \nabla_1) f_\alpha^{(0)}] [(\partial_{t1} + \mathbf{e}_\alpha \cdot \nabla_1) \tau_f] \} \\ &= -\frac{f_\alpha^{(2)}}{\tau_f} - \delta t^2 [(\tau_f - 1/2) (\partial_{t1} + \mathbf{e}_\alpha \cdot \nabla_1) F_{\alpha 1} \\ & - F_{\alpha 1} (\partial_{t1} + \mathbf{e}_\alpha \cdot \nabla_1) \tau_f]. \end{aligned} \quad (\text{A7})$$

Using Eqs. (A1), (A2), and (A4), the summation of Eq. (A5) multiplied by ε and Eq. (A7) multiplied by ε^2 gives

$$\begin{aligned} & \delta t (\partial_t + \mathbf{e}_\alpha \cdot \nabla) f_\alpha^{(0)} \\ &= -\frac{f_\alpha - f_\alpha^{\text{eq}}}{\tau_f} + \frac{2\tau_f - 1}{2\tau_f} F_\alpha \delta t + \delta t^2 (\tau_f - 1/2) \\ & \times [(\partial_t + \mathbf{e}_\alpha \cdot \nabla)^2 f_\alpha^{(0)} - (\partial_t + \mathbf{e}_\alpha \cdot \nabla) F_\alpha] \\ & + \delta t^2 \{ [(\partial_t + \mathbf{e}_\alpha \cdot \nabla) f_\alpha^{(0)}] [(\partial_t + \mathbf{e}_\alpha \cdot \nabla) \tau_f] \\ & - F_\alpha (\partial_t + \mathbf{e}_\alpha \cdot \nabla) \tau_f \} + O(\delta t^3). \end{aligned} \quad (\text{A8})$$

To define a restriction for distribution function f_α ,

$$\sum_\alpha f_\alpha = 0, \quad (\text{A9})$$

and define the velocity in the following form:

$$\mathbf{u} = \sum_\alpha f_\alpha \mathbf{e}_\alpha + \frac{\mathbf{F}}{2\rho} \delta t, \quad (\text{A10})$$

one can obtain the following relationships, according to Eq. (12):

$$\sum_\alpha f_\alpha = \sum_\alpha f_\alpha^{\text{eq}} = 0, \quad \sum_\alpha f_\alpha \mathbf{e}_\alpha - \sum_\alpha f_\alpha^{\text{eq}} \mathbf{e}_\alpha = -\frac{1}{2} \mathbf{F}' \delta t, \quad (\text{A11})$$

where $\mathbf{F}' = \mathbf{F}/\rho$. In addition, according to Eq. (15),

$$\sum_\alpha F_\alpha = 0; \quad \sum_\alpha F_\alpha \mathbf{e}_\alpha = \mathbf{F}'; \quad \sum_\alpha F_\alpha \mathbf{e}_\alpha \mathbf{e}_\alpha = \mathbf{0}. \quad (\text{A12})$$

Summing both sides of Eq. (A8) over α and using Eqs. (A11) and (A12) gives

$$\begin{aligned} \nabla \cdot \sum_\alpha f_\alpha^{(0)} \mathbf{e}_\alpha &= \delta t (\tau_f - 1/2) \left[2 \partial_t \nabla \cdot \sum_\alpha f_\alpha^{(0)} \mathbf{e}_\alpha + \nabla \cdot \left(\nabla \cdot \sum_\alpha f_\alpha^{(0)} \mathbf{e}_\alpha \mathbf{e}_\alpha \right) - \nabla \cdot \mathbf{F}' \right] \\ &+ \delta t \left[\left(\partial_t \sum_\alpha f_\alpha^{(0)} \mathbf{e}_\alpha + \nabla \cdot \sum_\alpha f_\alpha^{(0)} \mathbf{e}_\alpha \mathbf{e}_\alpha - \mathbf{F}' \right) \cdot \nabla \tau_f \right] + O(\delta t^2). \end{aligned} \quad (\text{A13})$$

Multiplying Eq. (A8) by \mathbf{e}_α and summing over α gives

$$\begin{aligned} & \partial_t \sum_\alpha f_\alpha^{(0)} \mathbf{e}_\alpha + \nabla \cdot \sum_\alpha f_\alpha^{(0)} \mathbf{e}_\alpha \mathbf{e}_\alpha \\ &= \delta t (\tau_f - 1/2) \left[\partial_t^2 \sum_\alpha f_\alpha^{(0)} \mathbf{e}_\alpha + 2 \partial_t \nabla \cdot \sum_\alpha f_\alpha^{(0)} \mathbf{e}_\alpha \mathbf{e}_\alpha + \nabla \cdot \left(\nabla \cdot \sum_\alpha f_\alpha^{(0)} \mathbf{e}_\alpha \mathbf{e}_\alpha \mathbf{e}_\alpha \right) - \partial_t \mathbf{F}' \right] \\ &+ \delta t \left[\left(\partial_t \sum_\alpha f_\alpha^{(0)} \mathbf{e}_\alpha + \nabla \cdot \sum_\alpha f_\alpha^{(0)} \mathbf{e}_\alpha \mathbf{e}_\alpha - \mathbf{F}' \right) \partial_t \tau_f + \left(\partial_t \sum_\alpha f_\alpha^{(0)} \mathbf{e}_\alpha \mathbf{e}_\alpha + \nabla \cdot \sum_\alpha f_\alpha^{(0)} \mathbf{e}_\alpha \mathbf{e}_\alpha \mathbf{e}_\alpha \right) \cdot \nabla \tau_f \right] + \mathbf{F}' + O(\delta t^2). \end{aligned} \quad (\text{A14})$$

Equations (A13) and (A14) indicate, respectively,

$$\nabla \cdot \sum_{\alpha} f_{\alpha}^{(0)} \mathbf{e}_{\alpha} = O(\delta t). \quad (\text{A15})$$

$$\partial_t \sum_{\alpha} f_{\alpha}^{(0)} \mathbf{e}_{\alpha} + \nabla \cdot \sum_{\alpha} f_{\alpha}^{(0)} \mathbf{e}_{\alpha} \mathbf{e}_{\alpha} = \mathbf{F}' + O(\delta t). \quad (\text{A16})$$

The substitution of Eqs. (A15) and (A16) into Eq. (A13) gives

$$\nabla \cdot \sum_{\alpha} f_{\alpha}^{(0)} \mathbf{e}_{\alpha} = 0 + O(\delta t^2). \quad (\text{A17})$$

Then, using the second relationship in Eqs. (12) and (A17) can be rewritten as

$$\nabla \cdot \mathbf{u} = 0 + O(\delta t^2). \quad (\text{A18})$$

Furthermore, according to Eqs. (A16) and (A14) can be reduced to

$$\begin{aligned} & \partial_t \sum_{\alpha} f_{\alpha}^{(0)} \mathbf{e}_{\alpha} + \nabla \cdot \sum_{\alpha} f_{\alpha}^{(0)} \mathbf{e}_{\alpha} \mathbf{e}_{\alpha} \\ &= \delta t \nabla \cdot \left[\left(\partial_t \sum_{\alpha} f_{\alpha}^{(0)} \mathbf{e}_{\alpha} \mathbf{e}_{\alpha} + \nabla \cdot \sum_{\alpha} f_{\alpha}^{(0)} \mathbf{e}_{\alpha} \mathbf{e}_{\alpha} \mathbf{e}_{\alpha} \right) \right. \\ & \quad \times (\tau_f - 1/2) \left. \right] + \mathbf{F}' + O(\delta t^2). \end{aligned} \quad (\text{A19})$$

Note that

$$\sum_{\alpha} f_{\alpha}^{(0)} \mathbf{e}_{\alpha i} \mathbf{e}_{\alpha j} \mathbf{e}_{\alpha k} = (\delta_{ij} \mathbf{u}_k + \delta_{ik} \mathbf{u}_j + \delta_{jk} \mathbf{u}_i) c_s^2 \quad (\text{A20})$$

and, using the second and the third relationships in Eqs. (12) and (A19) can be rewritten as

$$\begin{aligned} & \partial_t \mathbf{u} + \nabla \cdot (\mathbf{u} \mathbf{u} + p \mathbf{I}) \\ &= \delta t \nabla \cdot \{ [\partial_t (\mathbf{u} \mathbf{u}) + \partial_t p \mathbf{I}] + c_s^2 (\nabla \mathbf{u} + \mathbf{u} \nabla) \} (\tau_f - 1/2) \\ & \quad + \mathbf{F}' + O(\delta t^2). \end{aligned} \quad (\text{A21})$$

It is known that, in incompressible flows, pressure and velocity fluctuations are of the first and the second order of the Mach number [27,63,64]. Therefore,

$$\partial_t (\mathbf{u} \mathbf{u}) = O(\mathbf{u}^2) = O(\text{Ma}^2), \quad (\text{A22})$$

$$\partial_t p = O(\text{Ma}^2). \quad (\text{A23})$$

Thus, Eq. (A21) can be reduced to

$$\begin{aligned} \partial_t \mathbf{u} + \nabla \cdot (\mathbf{u} \mathbf{u} + p \mathbf{I}) &= \delta t \nabla \cdot [c_s^2 (\tau_f - 1/2) (\nabla \mathbf{u} + \mathbf{u} \nabla)] \\ & \quad + \mathbf{F}' + O(\delta t^2 + \text{Ma}^2 \delta t). \end{aligned} \quad (\text{A24})$$

Note that $\mathbf{F}' = \mathbf{F}/\rho$, where \mathbf{F} is defined in Eqs. (16) and (A24) can be rearranged as

$$\begin{aligned} \rho \partial_t \mathbf{u} + \rho \nabla \cdot (\mathbf{u} \mathbf{u}) &= -\nabla p_h + \nabla \cdot [\mu (\nabla \mathbf{u} + \mathbf{u} \nabla)] + \mathbf{F}_s + \mathbf{F}_b \\ & \quad + O(\delta t^2 + \text{Ma}^2 \delta t), \end{aligned} \quad (\text{A25})$$

where $\mu = \rho(\tau_f - 1/2)c_s^2 \delta t$ is the dynamic viscosity of the fluids.

It can be noted from Eqs. (A18) and (A25) that the lattice Boltzmann equation, Eq. (10), can recover the Navier-Stokes

equations (8a) and (8b) to the order of $O(\delta t^2)$ for the continuity equation and $O(\delta t^2 + \text{Ma}^2 \delta t)$ for the momentum equation.

Now, we discuss how to evaluate the microscopic pressure p on the basis of distribution function f_{α} . According to Eq. (13),

$$(1 - \omega_0) p(\mathbf{x}, t)/c_s^2 = -f_0^{\text{eq}}(\mathbf{x}, t) - \frac{\omega_0 |\mathbf{u}(\mathbf{x}, t)|^2}{2c_s^2}. \quad (\text{A26})$$

Thus,

$$\begin{aligned} (1 - \omega_0) p(\mathbf{x}, t)/c_s^2 &= -f_0(\mathbf{x}, t) + [f_0(\mathbf{x}, t) - f_0^{\text{eq}}(\mathbf{x}, t)] \\ & \quad - \frac{\omega_0 |\mathbf{u}(\mathbf{x}, t)|^2}{2c_s^2}. \end{aligned} \quad (\text{A27})$$

From Eq. (10), we have

$$f_0(\mathbf{x}, t + \delta t) - f_0(\mathbf{x}, t) = -[f_0(\mathbf{x}, t) - f_0^{\text{eq}}(\mathbf{x}, t)]/\tau_f. \quad (\text{A28})$$

Therefore,

$$\begin{aligned} f_0(\mathbf{x}, t) - f_0^{\text{eq}}(\mathbf{x}, t) &= -\tau_f [f_0(\mathbf{x}, t + \delta t) - f_0(\mathbf{x}, t)] \\ &= -\tau_f \delta t \partial_t f_0(\mathbf{x}, t) + O(\delta t^2). \end{aligned} \quad (\text{A29})$$

The equation above shows

$$f_0(\mathbf{x}, t) = f_0^{\text{eq}}(\mathbf{x}, t) + O(\delta t). \quad (\text{A30})$$

Substituting Eq. (A30) in to Eq. (A29), and using Eqs. (A22) and (A23) yields,

$$\begin{aligned} & f_0 - f_0^{\text{eq}} \\ &= -\tau_f \delta t [\partial_t f_0^{\text{eq}} + O(\delta t)] + O(\delta t^2) \\ &= \tau_f \delta t [(1 - \omega_0) \partial_t p + \omega_0 \partial_t |\mathbf{u}|^2 / 2] / c_s^2 + O(\delta t^2) \\ &= O(\text{Ma}^2 \delta t) + O(\delta t^2). \end{aligned} \quad (\text{A31})$$

Thus, the terms in square brackets in Eq. (A27) can be neglected as high order, and the pressure can be given by

$$p = (-f_0 c_s^2 - \omega_0 |\mathbf{u}|^2 / 2) / (1 - \omega_0) + O(\delta t^2 + \text{Ma}^2 \delta t). \quad (\text{A32})$$

An important step is to use Eq. (A9) so the restriction of $\sum_{\alpha} f_{\alpha} = 0$ is satisfied. Therefore, the pressure is evaluated using the following relationship rather than Eq. (A32).

$$p = \left(\sum_{\alpha \neq 0} f_{\alpha} c_s^2 - \omega_0 |\mathbf{u}|^2 / 2 \right) / (1 - \omega_0) + O(\delta t^2 + \text{Ma}^2 \delta t). \quad (\text{A33})$$

APPENDIX B: MULTISCALE ANALYSIS OF LBE FOR INTERFACE CAPTURING

In this section, the multiscaling analysis for the lattice Boltzmann equation (22) is performed by introducing the following expansions [56,62]:

$$g_{\alpha} = g_{\alpha}^{(0)}(\mathbf{x}, t) + \varepsilon g_{\alpha}^{(1)}(\mathbf{x}, t) + \varepsilon^2 g_{\alpha}^{(2)}(\mathbf{x}, t), \quad (\text{B1})$$

$$\partial_t = \varepsilon \partial_{t1} + \varepsilon^2 \partial_{t2}; \quad \nabla = \varepsilon \nabla_1. \quad (\text{B2})$$

Taylor series expansions of $g_\alpha(\mathbf{x} + \mathbf{e}_\alpha \delta t, t + \delta t)$ and $g_\alpha^{\text{eq}}(\mathbf{x} + \mathbf{e}_\alpha \delta t, t)$ in Eq. (22) to the second order yield

$$\begin{aligned} & \left[\delta t (\partial_t + \mathbf{e}_\alpha \cdot \nabla) + \frac{\delta t^2}{2} (\partial_t + \mathbf{e}_\alpha \cdot \nabla)^2 \right] g_\alpha \\ & - \eta \left[\delta t (\mathbf{e}_\alpha \cdot \nabla) + \frac{\delta t^2}{2} (\mathbf{e}_\alpha \cdot \nabla)^2 \right] g_\alpha^{\text{eq}} \\ & = -\frac{g_\alpha(\mathbf{x}, t) - g_\alpha^{\text{eq}}(\mathbf{x}, t)}{\tau_g} + O(\delta t^3). \end{aligned} \quad (\text{B3})$$

The substitution of Eqs. (B1) and (B2) into Eq. (B3) yields the Chapman-Enskog system as

$$O(\varepsilon^0) : g_\alpha^{(0)} = g_\alpha^{\text{eq}} + O(\delta t^3), \quad (\text{B4})$$

$$O(\varepsilon^1) : \delta t [\partial_{t1} + (1 - \eta) \mathbf{e}_\alpha \cdot \nabla_1] g_\alpha^{(0)} = -\frac{g_\alpha^{(1)}}{\tau_g}, \quad (\text{B5})$$

$$\begin{aligned} O(\varepsilon^2) : & \delta t [\partial_{t2} g_\alpha^{(0)} + (\partial_{t1} + \mathbf{e}_\alpha \cdot \nabla_1) g_\alpha^{(1)}] \\ & + \frac{\delta t^2}{2} [(\partial_{t1} + \mathbf{e}_\alpha \cdot \nabla_1)^2 - \eta (\mathbf{e}_\alpha \cdot \nabla_1)^2] g_\alpha^{(0)} \\ & = -\frac{g_\alpha^{(2)}}{\tau_g}. \end{aligned} \quad (\text{B6})$$

The substitution of Eq. (B5) into Eq. (B6) yields

$$\begin{aligned} & \delta t \partial_{t2} g_\alpha^{(0)} - \tau_g \delta t^2 (\partial_{t1} + \mathbf{e}_\alpha \cdot \nabla_1) [\partial_{t1} + (1 - \eta) \mathbf{e}_\alpha \cdot \nabla_1] g_\alpha^{(0)} \\ & + \frac{\delta t^2}{2} [(\partial_{t1} + \mathbf{e}_\alpha \cdot \nabla_1)^2 - \eta (\mathbf{e}_\alpha \cdot \nabla_1)^2] g_\alpha^{(0)} = -\frac{g_\alpha^{(2)}}{\tau_g}. \end{aligned} \quad (\text{B7})$$

Using Eqs. (B1), (B2), and (B4), Eq. (B5) $\times \varepsilon$ + Eq. (B7) $\times \varepsilon^2$ gives

$$\begin{aligned} & \varepsilon \delta t [\partial_{t1} + (1 - \eta) \mathbf{e}_\alpha \cdot \nabla_1] g_\alpha^{(0)} + \varepsilon^2 \delta t \partial_{t2} g_\alpha^{(0)} \\ & + \varepsilon^2 \delta t^2 [(1/2 - \tau_g) \partial_{t1}^2 + (-2\tau_g + \tau_g \eta + 1) \mathbf{e}_\alpha \cdot \nabla_1 \partial_{t1} \\ & + (1 - \eta)(1/2 - \tau_g) \mathbf{e}_\alpha \mathbf{e}_\alpha \nabla_1^2] g_\alpha^{(0)} = -\frac{\varepsilon g_\alpha^{(1)} + \varepsilon^2 g_\alpha^{(2)}}{\tau_g}. \end{aligned} \quad (\text{B8})$$

According to the expansions (B1), (B2), and (B4), Eq. (B8) can be reduced to

$$\begin{aligned} & [\partial_t + (1 - \eta) \mathbf{e}_\alpha \cdot \nabla] g_\alpha^{(0)} \\ & = \delta t [(\tau_g - 1/2) \partial_t^2 + (2\tau_g - \tau_g \eta - 1) \mathbf{e}_\alpha \cdot \nabla \partial_t \\ & + (1 - \eta)(\tau_g - 1/2) \mathbf{e}_\alpha \mathbf{e}_\alpha \nabla^2] g_\alpha^{(0)} - \frac{g_\alpha - g_\alpha^{\text{eq}}}{\tau_g \delta t} + O(\delta t^2). \end{aligned} \quad (\text{B9})$$

Summing both sides of Eq. (B9) over α and using $\sum_\alpha g_\alpha = \sum_\alpha g_\alpha^{\text{eq}}$ which is given by Eqs. (25) and (27),

$$\begin{aligned} & \partial_t \sum_\alpha g_\alpha^{(0)} + (1 - \eta) \nabla \cdot \sum_\alpha g_\alpha^{(0)} \mathbf{e}_\alpha \\ & = \delta t \left[(\tau_g - 1/2) \partial_t^2 \sum_\alpha g_\alpha^{(0)} + (2\tau_g - \tau_g \eta - 1) \partial_t \nabla \cdot \sum_\alpha g_\alpha^{(0)} \mathbf{e}_\alpha \right. \\ & \left. + (1 - \eta)(\tau_g - 1/2) \nabla \cdot \left(\nabla \cdot \sum_\alpha g_\alpha^{(0)} \mathbf{e}_\alpha \mathbf{e}_\alpha \right) \right] + O(\delta t^2). \end{aligned} \quad (\text{B10})$$

The equation above indicates

$$\partial_t \sum_\alpha g_\alpha^{(0)} + (1 - \eta) \nabla \cdot \sum_\alpha g_\alpha^{(0)} \mathbf{e}_\alpha = O(\delta t). \quad (\text{B11})$$

Using Eq. (B11), the first term and a part of the second term in square brackets in Eq. (B10) can be neglected as $O(\delta t^2)$. Thus,

$$\begin{aligned} & \partial_t \sum_\alpha g_\alpha^{(0)} + (1 - \eta) \nabla \cdot \sum_\alpha g_\alpha^{(0)} \mathbf{e}_\alpha \\ & = \delta t \left[(\tau_g - 1/2 - \eta/2) \partial_t \nabla \cdot \sum_\alpha g_\alpha^{(0)} \mathbf{e}_\alpha \right. \\ & \left. + (1 - \eta)(\tau_g - 1/2) \nabla \cdot \left(\nabla \cdot \sum_\alpha g_\alpha^{(0)} \mathbf{e}_\alpha \mathbf{e}_\alpha \right) \right] + O(\delta t^2). \end{aligned} \quad (\text{B12})$$

According to Eq. (23), $\eta = 2\tau_g - 1$, the first term in square brackets in Eq. (B12) equals zero. Then, substituting Eq. (25) into Eq. (B12) leads to

$$\frac{\partial \phi}{\partial t} + \nabla \cdot (\phi \mathbf{u}) = M \nabla^2 \mu_\phi + O(\delta t^2), \quad (\text{B13})$$

where $M = (\tau_g - 1/2) \Gamma \delta t$ is the mobility.

Using Eq. (A18), Eq. (B13) can be reduced to

$$\frac{\partial \phi}{\partial t} + \mathbf{u} \cdot \nabla \phi = M \nabla^2 \mu_\phi + O(\delta t^2). \quad (\text{B14})$$

APPENDIX C: BOUNDARY TREATMENT

This section describes the treatment of a few frequently used types of boundary conditions for the newly developed LBM. For this purpose, we consider a 2D or 3D channel flow in the x direction as shown in Fig. 19, where the top and bottom boundaries are either symmetrical or solid walls and the left and right boundaries are either periodical or velocity inlet and outlet, respectively.

1. Periodic boundary

The treatment for periodic boundary conditions is similar to that in traditional CFD, which requires relating the values

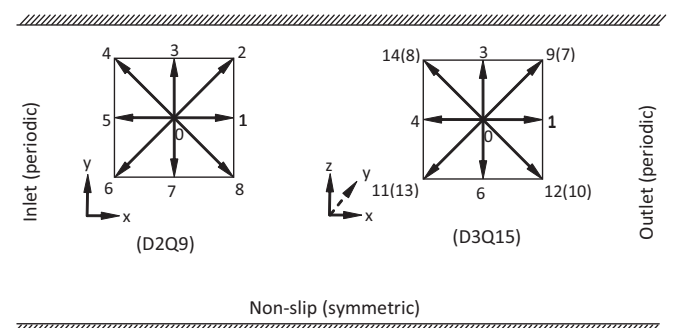


FIG. 19. Discrete velocity set of the D2Q9 model given by Eq. (11a) and the projection of the discrete velocity set of the D3Q15 model (y axis is vertically pointing into the paper) given by Eq. (11b) in a channel.

of the variables at the corresponding boundary of periodic condition to each other.

Equations (10) and (22) can be computed by the following two steps, i.e., collision and streaming.

Collision step:

$$f_\alpha^+(\mathbf{x}, t) = f_\alpha(\mathbf{x}, t) - \frac{f_\alpha(\mathbf{x}, t) - f_\alpha^{\text{eq}}(\mathbf{x}, t)}{\tau_f} + \frac{2\tau_f - 1}{2\tau_f} F_\alpha \delta t, \quad (\text{C1a})$$

$$\begin{aligned} g_\alpha^+(\mathbf{x}, t) &= g_\alpha(\mathbf{x}, t) - \frac{g_\alpha(\mathbf{x}, t) - g_\alpha^{\text{eq}}(\mathbf{x}, t)}{\tau_g} \\ &+ \eta [g_\alpha^{\text{eq}}(\mathbf{x} + \mathbf{e}_\alpha \delta t, t) - g_\alpha^{\text{eq}}(\mathbf{x}, t)]. \end{aligned} \quad (\text{C1b})$$

Streaming step:

$$f_\alpha(\mathbf{x}, t + \delta t) = f_\alpha^+(\mathbf{x} - \mathbf{e}_\alpha \delta t, t), \quad (\text{C2a})$$

$$g_\alpha(\mathbf{x}, t + \delta t) = g_\alpha^+(\mathbf{x} - \mathbf{e}_\alpha \delta t, t). \quad (\text{C2b})$$

At the boundaries, evaluating derivatives of the macroscopic quantities and implementation of the streaming step requires the information at $(\mathbf{x} - \mathbf{e}_\alpha)$, which is unavailable when \mathbf{e}_α is pointing into the computational domain. To provide this information, we define imaginary boundary nodes at $(\mathbf{x}_0 - \mathbf{n})$ and $(\mathbf{x}_\pi - \mathbf{n})$ given that the inlet and outlet boundary nodes are located at (\mathbf{x}_0) and (\mathbf{x}_π) , respectively. Here, \mathbf{n} is the unit vector normal to the boundary pointing to the computational domain. In the present case, as shown in Fig. 19, $\mathbf{n} = \mathbf{e}_1$ and $\mathbf{n} = -\mathbf{e}_1$ at the left and right boundaries, respectively. At the imaginary nodes,

$$f_\alpha^+(\mathbf{x}_0 - \mathbf{n}) = f_\alpha^+(\mathbf{x}_\pi), \quad f_\alpha^+(\mathbf{x}_\pi - \mathbf{n}) = f_\alpha^+(\mathbf{x}_0), \quad (\text{C3a})$$

$$g_\alpha^+(\mathbf{x}_0 - \mathbf{n}) = g_\alpha^+(\mathbf{x}_\pi), \quad g_\alpha^+(\mathbf{x}_\pi - \mathbf{n}) = g_\alpha^+(\mathbf{x}_0), \quad (\text{C3b})$$

$$\varphi(\mathbf{x}_0 - \mathbf{n}) = \varphi(\mathbf{x}_\pi), \quad \varphi(\mathbf{x}_\pi - \mathbf{n}) = \varphi(\mathbf{x}_0), \quad (\text{C3c})$$

where φ represents any of macroscopic quantizes, such as ϕ , ρ , μ_ϕ , and \mathbf{u} , which are used to evaluate their derivatives.

2. Symmetric boundary

The symmetric boundary is realized by setting the component of velocity and the gradients of any macroscopic variables normal to the boundary to be zero, i.e.,

$$\mathbf{n} \cdot \mathbf{u}|_{\mathbf{x}_s} = 0, \quad (\text{C4a})$$

$$\mathbf{n} \cdot \nabla \varphi|_{\mathbf{x}_s} = 0, \quad (\text{C4b})$$

where φ can be ϕ , ρ , μ_ϕ ; \mathbf{x}_s is the nodes at the symmetric boundary. According to Eq. (C4b), the normal-direction components of interfacial forces are zero and, thus, need not be calculated during the implement of boundary treatment. To apply the conditions to other quantities, we define a layer of imaginary nodes at $(\mathbf{x}_s - \mathbf{n})$,

$$f_\alpha^+(\mathbf{x}_s - \mathbf{n}) = f_{\tilde{\alpha}}^+(\mathbf{x}_s + \mathbf{n}), \quad (\text{C5a})$$

$$g_\alpha^+(\mathbf{x}_s - \mathbf{n}) = g_{\tilde{\alpha}}^+(\mathbf{x}_s + \mathbf{n}), \quad (\text{C5b})$$

$$\varphi(\mathbf{x}_s - \mathbf{n}) = \varphi(\mathbf{x}_s + \mathbf{n}), \quad (\text{C5c})$$

$$\begin{aligned} \mathbf{n} \cdot \mathbf{u}(\mathbf{x}_s - \mathbf{n}) &= -\mathbf{n} \cdot \mathbf{u}(\mathbf{x}_s + \mathbf{n}), \quad \boldsymbol{\tau} \cdot \mathbf{u}(\mathbf{x}_s - \mathbf{n}) \\ &= \boldsymbol{\tau} \cdot \mathbf{u}(\mathbf{x}_s + \mathbf{n}), \end{aligned} \quad (\text{C5d})$$

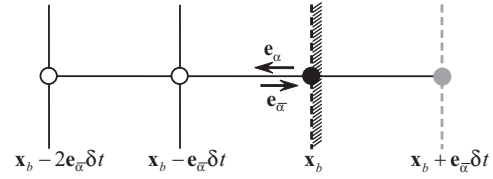


FIG. 20. Layout of the regularly spaced lattices and solid wall boundary (●: solid wall boundary node; ○: fluid nodes; ◐: imaginary solid nodes).

where $\mathbf{n} \cdot \mathbf{e}_{\tilde{\alpha}} = -\mathbf{n} \cdot \mathbf{e}_\alpha$, $\boldsymbol{\tau} \cdot \mathbf{e}_{\tilde{\alpha}} = \boldsymbol{\tau} \cdot \mathbf{e}_\alpha$, and $\boldsymbol{\tau}$ the unit vector in the tangential direction(s) of the boundary.

3. Nonslip stationary boundary

Consider a node at the bottom boundary as shown in Fig. 19, where the unknown distribution functions after the streaming step are those in the directions of $\alpha = 2, 3, 4$ and $\alpha = 3, 7, 8, 9, 14$ for the D2Q9 and D3Q15 models, respectively. To implement the nonslip boundary condition, we introduce imaginary solid nodes as shown in Fig. 20, where a solid wall (black dashed line) separates the solid region from the fluid region. The black solid circles (●), the open circles (○) and the gray solid circles (◐) denote the solid wall boundary node \mathbf{x}_b , fluid nodes, and imaginary solid nodes, respectively. After the streaming step, $f_\alpha(\mathbf{x}_b)$ and $g_\alpha(\mathbf{x}_b)$ are unknown.

First considering $f_\alpha(\mathbf{x}_b)$ and $g_\alpha(\mathbf{x}_b)$, we define a distribution function f'_α as

$$f'_\alpha = f_\alpha + \frac{1}{2} F_\alpha \delta t. \quad (\text{C6})$$

A particle distribution function bounce-back scheme [14] can be used for f'_α and g_α at the solid walls as illustrated in Fig. 20 to obtain no-slip velocity conditions. The basic idea of the bounce-back scheme is that when a particle distribution streams to a wall node, the particle distribution scatters back to the node it came from. Therefore, the unknown distribution functions coming from the solid part can be simply set to the known values of their corresponding ones with opposite directions, i.e., at node \mathbf{x}_b ,

$$f'_\alpha(\mathbf{x}_b) = f'_{\tilde{\alpha}}(\mathbf{x}_b), \quad (\text{C7a})$$

$$g_\alpha(\mathbf{x}_b) = g_{\tilde{\alpha}}(\mathbf{x}_b). \quad (\text{C7b})$$

In the above, $\mathbf{e}_{\tilde{\alpha}} \equiv -\mathbf{e}_\alpha$ as shown in Fig. 20.

Substituting Eq. (C6) into Eq. (C7a) gives

$$\begin{aligned} f_\alpha(\mathbf{x}_b) &= f_{\tilde{\alpha}}(\mathbf{x}_b) - [F_\alpha(\mathbf{x}_b) - F_{\tilde{\alpha}}(\mathbf{x}_b)]\delta t/2 \\ &= f_{\tilde{\alpha}}(\mathbf{x}_b) + F_{\tilde{\alpha}}(\mathbf{x}_b)\delta t. \end{aligned} \quad (\text{C8})$$

Next, introduce the boundary condition for the contact angle θ . When two-fluid interface meets a partially wetted solid wall, an order parameter derivative can be specified at the wall to control the contact angle. Following the argument set in Ref. [37], we assume that the fluid-solid interactions are sufficiently short-ranged such that their contribution can be calculated using a surface integral of the free-energy density of the system. Then, the following boundary condition can be obtained.

$$\mathbf{n} \cdot \nabla \phi|_{\mathbf{x}_b} = -\lambda/k \quad (\text{C9})$$

where λ is given by

$$\lambda = \Omega(\phi_A - \phi_B)^2 \sqrt{k\beta/8}. \quad (\text{C10})$$

In the above, Ω is a wetting potential represented as

$$\Omega = 2\text{sgn}\left(\frac{\pi}{2} - \theta\right) \left\{ \cos\left(\frac{\gamma}{3}\right) \left[1 - \cos\left(\frac{\gamma}{3}\right) \right] \right\}^{1/2}, \quad (\text{C11})$$

where $\gamma = \arccos(\sin^2 \theta)$ and $\text{sgn}(\xi)$ gives the sign of ξ .

Note that Eq. (C9) is valid only at equilibrium, and thus should not be imposed for the terms unrelated to the free energy [65]. Therefore, they are only be used to calculate μ_ϕ .

Finally, as shown in Fig. 20, evaluating first-order derivatives $\nabla\mu_\phi|_{x_b}$, $\nabla\rho|_{x_b}$ and $\nabla\mathbf{u}|_{x_b}$ using Eqs. (31a) and (31b) typically requires information at $(\mathbf{x}_b + \mathbf{e}_\alpha \delta t)$. To avoid unphysical mass and momentum fluxes across the wall boundary, the profiles of ρ and \mathbf{u} in the solid are assumed to have the mirror image of them in the fluid, i.e.,

$$\mu_\phi(\mathbf{x}_b + \mathbf{e}_\alpha \delta t) = \mu_\phi(\mathbf{x}_b - \mathbf{e}_\alpha \delta t), \quad (\text{C12})$$

$$\rho(\mathbf{x}_b + \mathbf{e}_\alpha \delta t) = \rho(\mathbf{x}_b - \mathbf{e}_\alpha \delta t), \quad (\text{C13})$$

$$\mathbf{u}(\mathbf{x}_b + \mathbf{e}_\alpha \delta t) = -\mathbf{u}(\mathbf{x}_b - \mathbf{e}_\alpha \delta t). \quad (\text{C14})$$

Note that Eqs. (C12) and (C13) give normal chemical potential and density gradients, respectively, at the plane boundary as

$$\mathbf{n} \cdot \nabla\mu_\phi|_{x_b} = 0, \quad \mathbf{n} \cdot \nabla\rho|_{x_b} = 0. \quad (\text{C15})$$

Thus, we have automatically ensured that $\mathbf{n} \cdot F_s|_{x_b} = \mathbf{n} \cdot F_p|_{x_b} = \mathbf{n} \cdot F_\mu|_{x_b} = 0$. During the implement of nonslip boundary condition, there is no need for explicitly calculating the normal-direction components of the interfacial forces.

Here, the nonslip boundary condition is approximated using a “full-way” bounce-back rule (with the wall located at the bounce-back nodes), so that the evaluation of interfacial force term can be simplified and also the method can be more easily extended to treat curved complex boundary as shown in Ref. [66]. As a penalty, this type of boundary treatment is of only the first-order accuracy. A “half-way” bounce-back scheme (with the wall placed half-way between a bounce-back node and a flow node) [67,68] combined with a suitable discretization scheme of the first-order derivatives and the Laplacian can achieve a second-order accuracy implementation of the non-slip boundary condition.

4. Velocity boundary

At the inlet boundary as shown in Fig. 19, the unknown density distribution functions after streaming are those in the directions of $\alpha = 2, 3, 4$ and $\alpha = 3, 7, 8, 9, 14$ for the D2Q9 and D3Q15 models, respectively.

According to Eqs. (12), (18a), and (C6), the velocity distribution function f'_α at the inlet boundary (\mathbf{x}_{in}) should satisfy the following momentum conservation condition:

$$\sum_\alpha f'_\alpha(\mathbf{x}_{in}) \mathbf{e}_\alpha = \sum_\alpha f_\alpha^{\text{eq}}(\mathbf{x}_{in}) \mathbf{e}_\alpha = \mathbf{u}_{in}, \quad (\text{C16})$$

where \mathbf{u}_{in} is the prescribed velocity at the inlet. If we use the bounce-back scheme for the nonequilibrium part of the particle

distribution functions f'_α , i.e.,

$$f'_\alpha(\mathbf{x}_{in}) - f_\alpha^{\text{eq}}(\mathbf{x}_{in}) = f'_{\bar{\alpha}}(\mathbf{x}_{in}) - f_{\bar{\alpha}}^{\text{eq}}(\mathbf{x}_{in}), \quad (\text{C17})$$

the momentum conservation in the direction normal to the boundary (x direction in the present case) can be satisfied. However, in the tangential direction(s), there is an excess of momentum of

$$\mathbf{M}(\mathbf{x}_{in}) = \sum_{\alpha \in \Lambda} \mathbf{e}_\alpha [f'_\alpha(\mathbf{x}_{in}) - f_\alpha^{\text{eq}}(\mathbf{x}_{in})], \quad (\text{C18})$$

where $\Lambda = \{\alpha | \mathbf{e}_\alpha \cdot \mathbf{n} = 0\}$. In order to ensure momentum conservation, we redistribute \mathbf{M} over the unknown distribution functions as proposed in Refs. [69,70],

$$f'_\alpha(\mathbf{x}_{in}) = f'_{\bar{\alpha}}(\mathbf{x}_{in}) + [f_\alpha^{\text{eq}}(\mathbf{x}_{in}) - f_{\bar{\alpha}}^{\text{eq}}(\mathbf{x}_{in})] - \frac{1}{Nc^2} \mathbf{e}_\alpha \cdot \mathbf{M}(\mathbf{x}_{in}), \quad (\text{C19})$$

where N is the number of the unknown f_α for which $\mathbf{e}_\alpha \cdot \boldsymbol{\tau} \neq 0$. Thus, $N = 2$ for the D2Q9 model, and $N = 4$ for the D3Q15 model.

According to Eqs. (25) and (27), the distribution functions g_α should satisfy the mass conservation condition at the inlet boundary as

$$\sum_\alpha g_\alpha(\mathbf{x}_{in}) = \sum_\alpha g_\alpha^{\text{eq}}(\mathbf{x}_{in}) = \phi_{in}, \quad (\text{C20})$$

where ϕ_{in} is the prescribed order parameter at the inlet. If we set the nonequilibrium part of the distribution function as

$$g_\alpha(\mathbf{x}_{in}) - g_\alpha^{\text{eq}}(\mathbf{x}_{in}) = -[g_{\bar{\alpha}}(\mathbf{x}_{in}) - g_{\bar{\alpha}}^{\text{eq}}(\mathbf{x}_{in})], \quad (\text{C21})$$

the following excess density appears:

$$\vartheta(\mathbf{x}_{in}) = \sum_{\alpha \in \Lambda} g_\alpha^{\text{neq}}(\mathbf{x}_{in}), \quad (\text{C22})$$

where $g_\alpha^{\text{neq}} = g_\alpha - g_\alpha^{\text{eq}}$ represents the nonequilibrium part of g_α . In order to find an exact match for Eq. (C20), the value of ϑ is redistributed over the unknown distribution functions as

$$g_\alpha(\mathbf{x}_{in}) = g_\alpha^{\text{eq}}(\mathbf{x}_{in}) - g_{\bar{\alpha}}^{\text{neq}}(\mathbf{x}_{in}), \quad \text{if } \mathbf{e}_\alpha \cdot \boldsymbol{\tau} = 0, \quad (\text{C23a})$$

$$g_\alpha(\mathbf{x}_{in}) = g_\alpha^{\text{eq}}(\mathbf{x}_{in}) - g_{\bar{\alpha}}^{\text{neq}}(\mathbf{x}_{in}) - \frac{\vartheta(\mathbf{x}_{in})}{N}, \quad \text{if } \mathbf{e}_\alpha \cdot \boldsymbol{\tau} \neq 0. \quad (\text{C23b})$$

One-sided biased differences can be used to evaluate of the first-order derivatives and the Laplacian of the macroscopic variables at the inlet. However, in most situations, the fluid flowing into the domain is of single phase and there is no two-fluids interface across the inlet boundary, and, hence, the evaluations of the derivatives of the macroscopic variable for the interfacial forces at the inlet can be avoided.

5. Free outflow boundary

For the Navier-Stokes fluids, several outflow conditions, such as the Neumann [71], the convective [72], and the do-nothing rule [73], are available. Here, we introduce only a

frequently used boundary condition, namely the zero Neumann boundary condition or free outflow condition [17]. Under this type of condition, the directional derivatives of independent variables in the normal direction of the outlet are zero. To implement the free out-flow boundary, we define a layer of imaginary nodes downstream the outlet. Assuming that the outlet boundary nodes are located at (\mathbf{x}_o) , then the imaginary boundary nodes are set at $(\mathbf{x}_o - \mathbf{n})$. At the imaginary

nodes,

$$f_\alpha^+(\mathbf{x}_o - \mathbf{n}) = f_\alpha^+(\mathbf{x}_o + \mathbf{n}), \quad g_\alpha^+(\mathbf{x}_o - \mathbf{n}) = g_\alpha^+(\mathbf{x}_o + \mathbf{n}), \quad (C24a)$$

$$\varphi(\mathbf{x}_o - \mathbf{n}) = \varphi(\mathbf{x}_o + \mathbf{n}), \quad (C24b)$$

where φ can be ϕ , ρ , p , μ_ϕ , and \mathbf{u} to provide information for evaluating first-order derivatives and the Laplacian at (\mathbf{x}_o) .

-
- [1] C. W. Hirt and B. D. Nichols, *J. Comput. Phys.* **39**, 201 (1981).
- [2] M. Sussman, P. Smereka, and S. Osher, *J. Comput. Phys.* **114**, 146 (1994).
- [3] G. Tryggvason, B. Bunner, A. Esmaeeli, D. Juric, N. Al-Rawahi, W. Tauber, J. Han, S. Nas, and Y. J. Jan, *J. Comput. Phys.* **169**, 708 (2001).
- [4] D. M. Anderson, G. B. McFadden, and A. A. Wheeler, *Annu. Rev. Fluid Mech.* **30**, 139 (1998).
- [5] D. Jacqmin, *J. Comput. Phys.* **155**, 96 (1999).
- [6] V. E. Badalassi, H. D. Ceniceros, and S. Banerjee, *J. Comput. Phys.* **190**, 371 (2003).
- [7] H. Ding, P. D. M. Spelt, and C. Shu, *J. Comput. Phys.* **226**, 2078 (2007).
- [8] H. W. Zheng, C. Shu, and Y. T. Chew, *Phys. Rev. E* **72**, 056705 (2005).
- [9] J. J. Huang, C. Shu, and Y. T. Chew, *Int. J. Numer. Methods Fluids* **60**, 203 (2009).
- [10] M. R. Swift, E. Orlandini, W. R. Osborn, and J. M. Yeomans, *Phys. Rev. E* **54**, 5041 (1996).
- [11] A. Fakhari and M. H. Rahimian, *Phys. Rev. E* **81**, 036707 (2010).
- [12] S. Succi, *The Lattice Boltzmann Equation for Fluid Dynamics and Beyond* (Oxford University Press, Oxford, 2001).
- [13] C. K. Aidun and J. R. Clausen, *Annu. Rev. Fluid Mech.* **42**, 439 (2010).
- [14] S. Chen and G. D. Doolen, *Annu. Rev. Fluid Mech.* **30**, 329 (1998).
- [15] G. Falcucci, S. Ubertini, C. Biscarini, S. Di Francesco, D. Chiappini, S. Palpacelli, A. De Maio, and S. Succi, *Commun. Comput. Phys.* **9**, 269 (2011).
- [16] X. Y. He, R. Y. Zhang, S. Y. Chen, and G. D. Doolen, *Phys. Fluids* **11**, 1143 (1999).
- [17] Y. Y. Yan and Y. Q. Zu, *Int. J. Heat Mass Transf.* **51**, 2519 (2008).
- [18] A. K. Gunstensen, D. H. Rothman, S. Zaleski, and G. Zanetti, *Phys. Rev. A* **43**, 4320 (1991).
- [19] D. H. Rothman and J. M. Keller, *J. Stat. Phys.* **52**, 1119 (1988).
- [20] D. Grunau, S. Y. Chen, and K. Eggert, *Phys. Fluids A* **5**, 2557 (1993).
- [21] X. W. Shan and H. D. Chen, *Phys. Rev. E* **47**, 1815 (1993).
- [22] M. R. Swift, W. R. Osborn, and J. M. Yeomans, *Phys. Rev. Lett.* **75**, 830 (1995).
- [23] A. N. Kalarakis, V. N. Burganos, and A. C. Payatakes, *Phys. Rev. E* **65**, 056702 (2002).
- [24] A. N. Kalarakis, V. N. Burganos, and A. C. Payatakes, *Phys. Rev. E* **67**, 016702 (2003).
- [25] T. Inamuro, T. Ogata, S. Tajima, and N. Konishi, *J. Comput. Phys.* **198**, 628 (2004).
- [26] X. Y. He, S. Y. Chen, and R. Y. Zhang, *J. Comput. Phys.* **152**, 642 (1999).
- [27] T. Lee and C. L. Lin, *J. Comput. Phys.* **206**, 16 (2005).
- [28] H. W. Zheng, C. Shu, and Y. T. Chew, *J. Comput. Phys.* **218**, 353 (2006).
- [29] J. W. Cahn and J. E. Hilliard, *J. Chem. Phys.* **28**, 258 (1958).
- [30] J. W. Cahn and J. E. Hilliard, *J. Chem. Phys.* **31**, 688 (1959).
- [31] J. S. Rowlinson and B. Widom, *Molecular Theory of Capillarity* (Clarendon, Oxford, 1989).
- [32] D. Jacqmin, *J. Fluid Mech.* **402**, 57 (2000).
- [33] Q. Li, K. H. Luo, Y. J. Gao, and Y. L. He, *Phys. Rev. E* **85**, 026704 (2012).
- [34] V. M. Kendon, M. E. Cates, I. Pagonabarraga, J.-C. Desplat, and P. Bladon, *J. Fluid Mech.* **440**, 147 (2001).
- [35] C. H. Shih, C. L. Wu, L. C. Chang, and C. A. Lin, *Philos. Trans. R. Soc. London A* **369**, 2510 (2011).
- [36] O. Penrose and P. C. Fife, *Physica D* **43**, 44 (1990).
- [37] Y. Y. Yan and Y. Q. Zu, *J. Comput. Phys.* **227**, 763 (2007).
- [38] D. Jamet, D. Torres, and J. U. Brackbill, *J. Comput. Phys.* **182**, 262 (2002).
- [39] Z. L. Guo, B. C. Shi, and N. C. Wang, *J. Comput. Phys.* **165**, 288 (2000).
- [40] Z. L. Guo, B. C. Shi, and C. G. Zheng, *Int. J. Numer. Methods Fluids* **39**, 325 (2002).
- [41] K. Langaas and J. M. Yeomans, *Eur. Phys. J. B* **15**, 133 (2000).
- [42] A. V. Coward, Y. Y. Renardy, M. Renardy, and J. R. Richards, *J. Comput. Phys.* **132**, 346 (1997).
- [43] T. Lee and P. F. Fischer, *Phys. Rev. E* **74**, 046709 (2006).
- [44] X. Shan, *Phys. Rev. E* **73**, 047701 (2006).
- [45] Z. L. Guo, C. G. Zheng, and B. C. Shi, *Phys. Rev. E* **83**, 036707 (2011).
- [46] S. T. Zalesak, *J. Comput. Phys.* **31**, 335 (1979).
- [47] S. V. Lishchuk, C. M. Care, and I. Halliday, *Phys. Rev. E* **67**, 036701 (2003).
- [48] C. M. Pooley and K. Furtado, *Phys. Rev. E* **77**, 046702 (2008).
- [49] K. N. Premnath and J. Abraham, *Phys. Rev. E* **71**, 056706 (2005).
- [50] W. R. Osborn, E. Orlandini, M. R. Swift, J. M. Yeomans, and J. R. Banavar, *Phys. Rev. Lett.* **75**, 4031 (1995).
- [51] J. Chin and P. V. Coveney, *Phys. Rev. E* **66**, 016303 (2002).
- [52] A. G. Xu, G. Gonnella, and A. Lamura, *Physica A* **331**, 10 (2004).
- [53] H. B. Huang, L. Wang, and X. Y. Lu, *Comput. Math. Appl.* **61**, 3606 (2011).
- [54] T. Reis and T. N. Phillips, *J. Phys. A: Math. Theor.* **40**, 4033 (2007).
- [55] S. Leclaire, M. Reggio, and J.-Y. Trépanier, *Appl. Math. Model.* **36**, 2237 (2012).

- [56] J. M. Buick and C. A. Greated, *Phys. Rev. E* **61**, 5307 (2000).
- [57] G. Tryggvason, *J. Comput. Phys.* **75**, 253 (1988).
- [58] J. L. Guermond and L. Quartapelle, *J. Comput. Phys.* **165**, 167 (2000).
- [59] L. Lee, *Comput. Fluids* **39**, 1022 (2010).
- [60] D. Chiappini, G. Bella, S. Succi, F. Toschi, and S. Ubertini, *Commun. Comput. Phys.* **7**, 423 (2010).
- [61] D. Chiappini, G. Bella, S. Succi, and S. Ubertini, *Int. J. Mod. Phys. C* **20**, 1803 (2009).
- [62] Z. L. Guo, C. G. Zheng, and B. C. Shi, *Phys. Rev. E* **65**, 046308 (2002).
- [63] M. S. Day and J. B. Bell, *Combust. Theory Modelling* **4**, 535 (2000).
- [64] T. Lee and C.-L. Lin, *Phys. Rev. E* **67**, 056703 (2003).
- [65] T. Lee and L. Liu, *J. Comput. Phys.* **229**, 8045 (2010).
- [66] X. D. Niu, T. Munekata, S. A. Hyodo, and K. Suga, *J. Power Sources* **172**, 542 (2007).
- [67] Q. S. Zou, S. L. Hou, and G. D. Doolen, *J. Stat. Phys.* **81**, 319 (1995).
- [68] X. Y. He, Q. S. Zou, L. S. Luo, and M. Dembo, *J. Stat. Phys.* **87**, 115 (1997).
- [69] R. S. Maier, R. S. Bernard, and D. W. Grunau, *Phys. Fluids* **8**, 1788 (1996).
- [70] Q. S. Zou and X. Y. He, *Phys. Fluids* **9**, 1591 (1997).
- [71] H. Abbassi, S. Turki, and S. B. Nasrallah, *Comput. Mech.* **28**, 10 (2002).
- [72] A. Sohankar, C. Norberg, and L. Davidson, *Int. J. Numer. Methods Fluids* **26**, 39 (1998).
- [73] J. G. Heywood, R. Rannacher, and S. Turek, *Int. J. Numer. Methods Fluids* **22**, 325 (1996).